PHYSICAL REVIEW MATERIALS **9**, 124413 (2025)

Ge-based clinopyroxene series: First principles and experimental local probe study

Ricardo P. Moreira,[1] E. Lora da Silva,[1,2] Gonçalo N. P. Oliveira,[1] P. Neenu Lekshmi,[1] Pedro Rocha-Rodrigues,[1]
Fábio G. Figueiras,[1] Abderrazzak Ait Bassou,[3] Alessandro Stroppa,[4] Claire V. Colin,[5] Céline Darie,[5] João G. Correia,[6]
Lucy V. C. Assali,[7] Helena M. Petrilli,[7] Armandina M. L. Lopes,[1] and João P. Araújo[1,*]

[1]*IFIMUP, Institute of Physics for Advanced Materials, Nanotechnology and Photonics, Departamento de Física e Astronomia da Faculdade de Ciências da Universidade do Porto, Rua do Campo Alegre s/n, 4169-007 Porto, Portugal*
[2]*High Performance Computing Chair, University of Évora, Rua Romão Ramalho 59, 7000-671 Évora, Portugal*
[3]*CQ-VR Centro de Química Vila Real, School of Science and Technology (ECT), Physics Department, Universidade de Trás-os-Montes e Alto Douro, 5000-801 Vila Real, Portugal*
[4]*CNR-SPIN c/o Università degli Studi dell'Aquila, Via Vetoio 10, 67010 Coppito, L'Aquila, Italy*
[5]*Université Grenoble Alpes, CNRS, Institut Néel, 38000 Grenoble, France*
[6]*C2TN, DECN, Instituto Superior Técnico, Universidade de Lisboa, Bobadela, Portugal*
[7]*Instituto de Física, Universidade de São Paulo, CP 66318, 05315-970 São Paulo-SP, Brazil*

(Received 1 August 2024; accepted 24 September 2025; published 26 December 2025)

The electronic properties of the Ca/Sr and Mn site substitution of $CaMnGe_2O_6$ and $SrMnGe_2O_6$ clinopyroxene systems have been investigated by *ab initio* calculations within the density functional theory (DFT) framework, using on-site Hubbard U to describe the highly correlated Mn $3d$ states and a hybrid exchange-correlation functional to obtain the energy band-gap values. Compositions such as $(Ca, Sr)_{1-x}Cd_xMnGe_2O_6$ and $(Ca, Sr)Mn_{1-x}Cd_xGe_2O_6$ (where $x = 0.125, 0.25$) are predicted to be stable. Also, we proved that implanted Cd impurity could indeed replace either the Ca/Sr or the Mn sites in the crystalline structures. These findings were obtained by combining first principles electric field gradient calculations, using a supercell scheme, with experimental time-differential perturbed angular correlation results. Additionally, DFT calculations showed that Cd substitution is expected to lead to a reduction in the band-gap width. Cd-doped systems were successfully synthesized and experimental results evidencing opportunities for potential band-gap engineering are reported.

DOI: 10.1103/ms66-db9b

I. INTRODUCTION

Pyroxenes are a class of materials with general formula AMX_2O_6, where A is a monovalent or a divalent cation, M is, respectively, a trivalent or a divalent cation, and X is typically either Si or Ge. They are well-known in mineralogy and geology as they are one of the main rock-forming minerals of Earth's crust [1]. Within this rich family of compounds, monoclinic pyroxenes (clinopyroxenes), with a $3d$ transition metal at the M site, have recently been a subject of interest in the field of condensed matter physics due to the diversity of their magnetic properties, namely, multiferroicity in $SrMnGe_2O_6$ [2,3] and $NaFe(Si/Ge)_2O_6$ [4,5], magnetoelectric effect in $CaMnGe_2O_6$ [6] and $Li(Cr/Fe)Si_2O_6$ [4], and ferrotoroidal ordering in $LiFeSi_2O_6$.

In spite of their natural prevalence, pyroxenes have not been the subject of many computational or theoretical investigations. It is notewort5hy of mentioning that density functional theory (DFT) studies [7] have shown that substitution of Al^{3+} by Tl^{3+} in $NaAlSi_2O_6$ results in a reduction in the band-gap width from 5.32 eV to 2.05 eV. A further reduction is observed when replacing Na by the organic cation CH_3SH_2, showing the high tunability of the band gap in these materials. Other works have shown their potential usefulness in batteries, demonstrating that pyroxenes $CaFe/MnSi_2O_6$ could display high theoretical energy densities in Ca-based batteries [8], whereas $LiFeSi_2O_6$ has been shown to undergo a reversible electrochemical reaction against Li, thus exhibiting potential for use as an electrode material in Li-ion batteries [9]. Recently, published works have studied pyroxenes bearing Co at the M site, with these materials having been found to be a good platform for studying the dynamically intertwined lattice, orbital, charge, and spin degrees of freedom in the quantum regime [10], as well as for the Kitaev model [11]. The magnetic properties of $CaMnGe_2O_6$ were studied by Temnikov *et al.* [12] who computed the exchange parameters and showed that the magnetic frustration in the system is weak, which could explain the frequent occurrence of commensurate collinear antiferromagnetic (AFM) structures in Ca^{2+}-bearing pyroxenes. Structural, mechanical, electronic, optical, and thermal properties of $CaTGe_2O_6$ ($T =$ Mn, Fe, Co) were studied by Akter *et al.* [13], who, based on their findings, suggested that these systems may prove useful for spintronics or optoelectronics applications in the future. Lastly, Fakhera *et al.* [14] studied the $SrYGe_2O_6$ ($Y =$ Mn, Fe, Co) clinopyroxenes, studying their structural, mechanical, magnetic, and optoelectronic properties, determining, based on the properties found, that these point to possible use in the context of spintronics or optoelectronics. When the M site is occupied by a magnetic cation, such an arrangement leads to low-dimensional magnetic properties and to magnetic

---

[*] Contact author: jearaujo@fc.up.pt

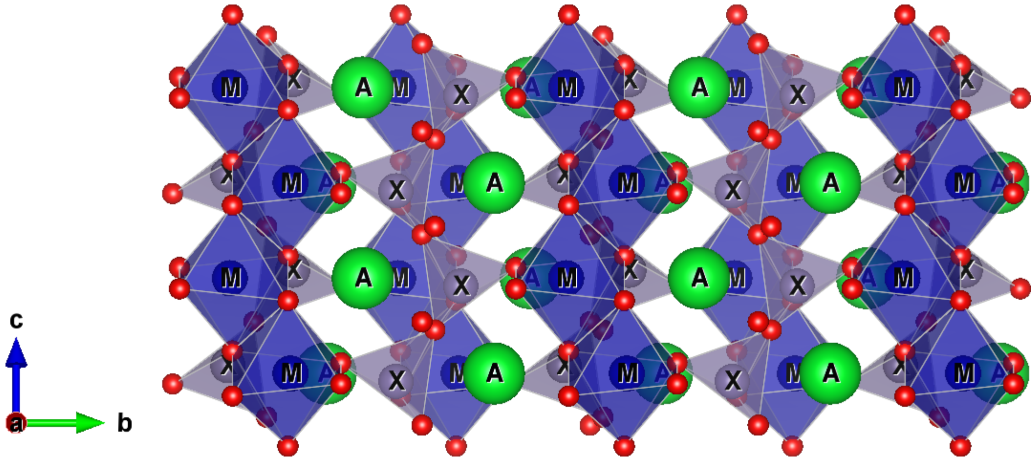

FIG. 1. Representation of the AMnGe$_2$O$_6$ clinopyroxene structure. Red spheres represent the oxygen sites, green spheres the A cation sites, grey tetrahedra the Ge-site coordination polyhedra, and blue octahedra the Mn-site coordination polyhedra.

frustration due to the competition between interchain and intrachain interactions [4]. It is the existence and the possible interplay between the low dimensionality and frustration that is thought to give rise to the aforementioned diversity of magnetic properties in these materials [6]. Moreover, it has been suggested that the magnetic frustration can lead to spin spiral structures, which may be favourable towards magnetically driven ferroelectricity, making these compounds good candidates for multiferroic behavior [4]. The AMnGe$_2$O$_6$ germanate clinopyroxene series is here explored, with the A site occupied by group-II elements from the periodic table, namely, Be, Mg, Ca, and Sr. *Ab initio* calculations in the DFT framework performed here demonstrated that the compounds containing Be and Mg are not stable, explaining the absence of experimental results in the literature. Further examination of compositions such as (Ca, Sr)$_{1-x}$Cd$_x$MnGe$_2$O$_6$ and (Ca, Sr)Mn$_{1-x}$Cd$_x$Ge$_2$O$_6$ (where $x = 0.125, 0.25$) was first conducted using *ab initio* computational simulations, which enabled the prediction of the phase stability of these alloys. Subsequently, time-differential perturbed angular correlation (TDPAC) spectroscopy, a nuclear local probe technique, was used, after Cd ion implantation, to infer the electric field gradient (EFG) at a given Cd nuclear site. Additionally, DFT simulations were conducted to determine the local environments of the Cd probes in CaMnGe$_2$O$_6$ and SrMnGe$_2$O$_6$ systems. After experimentally confirming that Cd can occupy both the Ca/Sr and Mn sites, the band gaps of these alloys were estimated, using both DFT with an on-site Hubbard U and the hybrid Heyd–Scuseria–Ernzerhof (HSE06) functional; the effective masses of the electrons and holes were also analyzed. We report the optical absorption and band gap of germanate clinopyroxenes through diffuse reflectance spectroscopy and compare the results with advanced DFT calculations. To investigate the fundamental effect of atomic substitution in CaMnGe$_2$O$_6$ and SrMnGe$_2$O$_6$ systems by atoms of similar ionic radius, but distinct ionic structure, we used the insight gained from the TDPAC and DFT results to synthesize the Cd-doped germanate clinopyroxenes. This led to an initial study of these compounds, further expanding the understanding of their optical properties. The diffuse reflectance measurements show the possibility of tuning the band gap through Cd doping, highlighting its potential applications in various fields.

II. METHODS

A. Computational methodology

The ground state structure for the AMnGe$_2$O$_6$ clinopyroxenes is a monoclinic Bravais lattice with space group $C2/c$ (No. 15), where the Mn cations are in octahedral sites (Wyckoff 4e atomic positions), the A cations are in 8-coordinated sites (Wyckoff 4e atomic positions) and the Ge-cations are in tetrahedral sites (Wyckoff 8f atomic positions). Their structure is characterized by quasi-one-dimensional chains with edge-sharing MnO$_6$ octahedra running along the c axis, and connected by corner-sharing GeO$_4$ tetrahedra, along the c axis, as schematically represented in Fig. 1.

DFT calculations were performed using the Quantum Espresso (QE) suite [15,16], with projector-augmented wave datasets [17,18]. The generalized gradient approximation with Perdew-Burke-Ernzerhof (PBE) parametrization [19] was used to describe the exchange-correlation functional. The atomic valence configurations were Be[$2s^2$], Mg[$2s^2 2p^6 3s^2$], Ca[$3s^2 3p^6 4s^2$], Sr[$4s^2 4p^6 5s^2$], Mn[$3s^2 3p^6 3d^5 4s^2$], Ge[$3d^{10} 4s^2 4p^2$], O[$2s^2 2p^4$], and Cd[$4d^{9.5} 5s^2 5p^{0.5}$]. The kinetic energy cutoffs were 70 and 540 Ry for, respectively, the wave functions and charge densities, values that were raised to 113 and 900 Ry for the EFG calculations. The Brillouin zone (BZ) was sampled by a $(9 \times 9 \times 18)$ Monkhorst-Pack **k**-point grid. To treat the strongly correlated Mn-3d states, an effective on-site Hubbard $U = 4$ eV potential was considered [20–22], and this is the value used throughout this paper whenever PBE + U calculations are mentioned. For an accurate description of the energy band gap values, we employed the hybrid HSE06 functional [23] at the relaxed structures obtained from the PBE + U calculations. Ground-state properties were obtained through total energy minimizations with respect to both atomic positions and cell parameters. Forces in any ion were converged to lower than 0.05 eV/Å. Variable cell shape relaxations were performed using the damped Beeman ionic dynamics and the Wentzcovitch extended Lagrangian [24–26]. The $A\mathrm{MnGe_2O_6}$ enthalpies of formation were determined by the DFT total energies of the compounds and the respective total energies of the $A\mathrm{GeO_3}$ and $\mathrm{MnGeO_3}$ stable constituent oxides accordingly to Eq. (A1) in Appendix A, demonstrating that only the Ca and Sr-related compounds are stable. To simulate the Cd substitution on either A or Mn cation sites, when necessary, an $1 \times 1 \times 2$ supercell was constructed and a $(9 \times 9 \times 9)$ **k**-point grid was used to sample the BZ. The EFGs, computed by the Gauge Including Projector Augmented Waves [27] package routine implemented in QE, were evaluated at the Sr, Ca, Mn, Ge, O, and Cd nuclear sites.

B. Experimental methods

1. Ion implantation and time-differential perturbed angular correlation spectroscopy

To infer if Cd can effectively substitute a regular position in the crystal structures, ion implantation followed by EFG measurements can be used. The experimental values of the EFG can be obtained via TDPAC spectroscopy. For this purpose, pelletized samples of $\mathrm{SrMnGe_2O_6}$ and $\mathrm{CaMnGe_2O_6}$ materials, from Refs. [2,6] were implanted at ISOLDE-CERN by a 30 keV beam of $^{111\mathrm{m}}$Cd probes ($^{111\mathrm{m}}\mathrm{Cd} \rightarrow {}^{111}\mathrm{Cd}, t_{1/2} = 48.6$ minutes), which have a nuclear spin $I = 5/2$ and an electric quadrupole moment $Q = 0.83(13)$ b in the intermediate state of decay [28]. Small doses of the order of 10^{11} atoms/cm^2 were implanted and subsequently an annealing was performed at a temperature of ~1123 K for 20 minutes in air to recover from implantation damage. Confirmation for the recovery of point defects and for the incorporation of Cd into the lattice was given by the TDPAC measurements themselves, which yielded well-defined experimental $R(t)$ anisotropy functions. The measurements were performed on 6-$\mathrm{BaF_2}$ detectors TDPAC spectrometers [29], equipped with either a closed-cycle cryostat or a special high-temperature furnace for temperature control. The experimental $R(t)$ function was fitted with exact numerical methods that build the expected observable by solving the hyperfine interaction Hamiltonian's characteristic equations [30–34]. The EFG, that characterizes the surrounding charge density that interacts with a probe nucleus, can be represented as a rank-2 symmetric and traceless tensor. As such it is always possible to be diagonalized into the principal axis system. The experimentally observable EFG is conventionally described by only two parameters namely: the principal component V_{zz} and the asymmetry parameter η defined as

$$\eta = \frac{V_{xx} - V_{yy}}{V_{zz}}. \tag{1}$$

The EFG principal axis tensor components V_{zz}, V_{yy}, and V_{xx} are defined such that $|V_{zz}| \geqslant |V_{yy}| \geqslant |V_{xx}|$ [30].

The signature for the interaction between the probe atoms and their local environment is the perturbation function $G_{kk}(t)$. In the case of static electric quadrupole interactions, the interaction can be written as [35]

$$G_{kk}(t) = \sum_n s_{k_n} \cos(\omega_n t) e^{-\delta\omega_n t/2}, \tag{2}$$

where s_{k_n} is a function of η and ω_n is a function of both η and the fundamental frequency ω_Q. The exponential term arises from randomly distributed defects and lattice strains that result in an attenuation of the experimental $R(t)$ function. In the case of the $^{111\mathrm{m}}$Cd probes, the intermediate level in the decay has a nuclear spin of $I = 5/2$, which leads to a split of the intermediate level into three sublevels due to the quadrupole interaction and three transition frequencies, ω_1, ω_2, and $\omega_3 = \omega_1 + \omega_2$. The fundamental frequency is usually defined as [30]

$$\omega_Q = \frac{eQV_{zz}}{4I(2I-1)\hbar}, \tag{3}$$

where Q is the nuclear quadrupole moment, e is the electron charge, and $\hbar$ is the reduced Planck's constant. In the case of static interactions, the experimental anisotropy function can be written as

$$R(t) = \sum A_{kk} G_{kk}(t) \tag{4}$$

where A_{kk} are the anisotropy coefficients for the nuclear decay cascade.

2. Sample synthesis

Proceeding akin to what had previously been reported for the parent compounds, $\mathrm{CaMnGe_2O_6}$ [6] and $\mathrm{SrMnGe_2O_6}$ [2], and guided by DFT calculations and TDPAC measurements, which indicate the stability of these compounds upon Cd doping at the Ca/Sr and Mn sites, the $\mathrm{Ca_{1-x}Cd_xMnGe_2O_6}$, $\mathrm{CaMn_{1-x}Cd_xGe_2O_6}$, $\mathrm{Sr_{1-x}Cd_xMnGe_2O_6}$, and $\mathrm{SrMn_{1-x}Cd_xGe_2O_6}$ compounds ($x = 0.125, 0.25$) were synthesized following the solid-state reaction method. For the Ca/Sr-based clinopyroxenes, stoichiometric quantities of $\mathrm{CaCO_3}$ (99%)/$\mathrm{SrCO_3}$ (99.995%), CdO (99.99%), MnO (99%), and $\mathrm{GeO_2}$ (99.998%) were hand ground together and the powder fired in air at 1373 K for 50 h with a heating and cooling rate of 10 K/min. The resulting powder was reground and pelletized, then sintered for 12 h under the same conditions for Sr-based clinopyroxenes and at 1073 K for 4 h in air for Ca-based clinopyroxenes. Pristine samples were synthesized following Refs. [2,6].

The phase purity of the synthesized samples were assessed by monitoring the powder x-ray diffraction data collected using Rigaku SmartLab diffractometer (45 kV, 200 mA) operating with Cu Kα in Bragg-Brentano geometry. Crystal structure analysis was performed using Fullprof software [36–38], the corresponding structural refinement plots and structural parameters are provided in Appendix B.

3. Reflectometry

To inspect the band-gap widths, diffuse reflectance measurements were acquired using CARY 50 Varian spectrophotometer in a range from 200 to 1000 nm, and the $\mathrm{BaSO_4}$ standard compound as the white background reference. The acquired spectrum was converted using the Kubelka-Munk function [39], where the magnitude $F(R_\infty)$ was proportional to the absorption coefficient (α). The optical band gap (E_g) was calculated following the relation presented by Tauc and expressed by Davis and Mott [40–42]: $(\alpha E)^{\frac{1}{n}} = (h\nu - E_g)$, where $E = h\nu$ is the photon energy and E_g is the optical

TABLE I. Experimental [2,6] and theoretical lattice parameters for $SrMnGe_2O_6$ and $CaMnGe_2O_6$ compounds obtained using the PBE and PBE + U approximations.

System	Research type	a (Å)	b (Å)	c (Å)	β (deg)
$SrMnGe_2O_6$	Experimental	10.3511(6)	9.4204(5)	5.5093(3)	104.700(2)
	Theoretical PBE	10.5295	9.4912	5.5992	105.029
	Theoretical PBE + U	10.5638	9.5795	5.6230	104.906
$CaMnGe_2O_6$	Experimental	10.2794(3)	9.1756(3)	5.4714(2)	104.244(2)
	Theoretical PBE	10.4006	9.2248	5.5194	103.921
	Theoretical PBE + U	10.4495	9.3204	5.5472	104.109

band gap energy. The power-law exponent, n, depends on the transition type: $n = \frac{1}{2}$ for a direct E_g and $n = 2$ for an indirect E_g. The value of indirect or direct E_g is estimated by plotting $(\alpha h\nu)^{\frac{1}{2}}$ or $(\alpha h\nu)^2$, respectively, as a function of the photon energy and extrapolating it to $\alpha = 0$ [43].

III. RESULTS AND DISCUSSION

A. Density functional theory calculations

To ascertain the possibility of synthezing other compounds in the AMnGe$_2$O$_6$ series (A = Be, Mg, Ca, Sr), the enthalpy of formation from constituent oxides of the series has been examined through DFT calculations. As mentioned before, we have determined that only the $CaMnGe_2O_6$ and $SrMnGe_2O_6$ clinopyroxene compounds are thermodynamically stable. This is evidenced by their respective –0.19 and –0.11 eV/f.u. (negative) enthalpies of formation, calculated through Eq. (A1) (Appendix A). On the other hand, both $BeMnGe_2O_6$ and $MgMnGe_2O_6$ presented 0.12 eV/f.u. (positive) enthalpies of formation, supporting that these are not stable against dissociation into the respective stable constituent oxides: $BeGeO_3$ or $MgGeO_3$ and $MnGeO_3$. These results are consistent with the fact that only the former two compounds have been experimentally synthesized, whereas the synthesis of the latter two has not yet been reported. Such observation implies that different reaction pathways toward synthesis will still have to be explored in order to possibly realize experimentally the compounds containing Be and Mg.

Table I summarizes the calculated lattice parameters for the $SrMnGe_2O_6$ and $CaMnGe_2O_6$ systems, computed with both the PBE and PBE + U (using $U = 4$ eV) approximations, as well as the experimental values reported in the literature [2,6]. Regarding the $SrMnGe_2O_6$ system, we can observe that the lattice parameters computed with the PBE functional are overestimated, with respect to the experimental values, corresponding to a relative increase of ∼1.7%, ∼0.8%, and ∼1.6%, respectively, for a, b, and c parameters, which is in line with the well-known tendency of the PBE functional [44]. As compared to the lattice parameters likewise computed with the PBE functional for this system by Fakhera *et al.* [14], the values we obtained for the lattice parameters are 0.6–1.2% smaller, with the difference likely being owed to the difference in magnetic ordering, which in our case was considered as AFM, as is observed experimentally, whereas the aforementioned work considered a ferromagnetic (FM) configuration for their calculations. The inclusion of the on-site effective Hubbard-U potential results in a further relative increase of these parameters with ∼2.1%, ∼1.7%, and ∼2.1%, when compared to the experimental values. Though the β monoclinic angle is overestimated for both PBE and PBE + U approximations, when comparing to experimental data, the difference is in fact smaller when considering the PBE + U calculations, resulting in a value closer to the experimental one. In the case of $CaMnGe_2O_6$, the a and b theoretical lattice parameters obtained from PBE calculations likewise are overestimated, relative to experimental data, by ∼1.2% and ∼0.5%, respectively. On the other hand, we observed that the c parameter is underestimated by ∼0.9%. The lattice parameters calculated with the PBE functional by Akter *et al.* [13] are in quite good agreement with the ones we found, differing by less than 0.1%, with the exception of the b parameters, which is 1.1% larger than ours. Analogously to what was observed for $SrMnGe_2O_6$, the a and b lattice parameters that resulted from the PBE + U approach display an increase with respect to the PBE values, presenting an overestimation of ∼1.7% and ∼1.6%, respectively, relative to the experimental results; whereas the c parameter is still underestimated, though smaller than the one obtained by the PBE functional of ∼0.4%. Also, and distinctly from what was observed for $SrMnGe_2O_6$, the theoretical monoclinic angle is underestimated in relation to the experimental angle, though again, results from the PBE + U approximation are closer to the experimental value.

The $CaMnGe_2O_6$ and $SrMnGe_2O_6$ projected density of states (PDOS), obtained considering the PBE calculations (without the Hubbard-U correction), were computed and are displayed in Fig. 2, in which the valence band maximum (VBM) is aligned at the Fermi energy and is set to zero. Two narrow bands form the VBM region, being mainly composed by the split of the Mn-3d derived bonding states, hybridized with a smaller contribution from the O-p states. Energetically below these narrow bands (< –2.5 eV), a broader band is observed and it is mostly dominated by the O-p states, with a very small mixture of Mn-3d states. The conduction band minimum (CBM) region, on the other hand, presents low density of states and hybridization between the O-p and Ge-p states. For increasing energies, the DOS significantly increases, forming a narrow resonant band, between 2.0 and 3.0 eV, that is mainly composed by the unoccupied Mn-3d states. For both studied systems, the PDOS are qualitatively very similar, although at the conduction band region the observed Mn resonant peaks for $SrMnGe_2O_6$ are broader when compared to those of $CaMnGe_2O_6$.The electronic band gaps are also noted to be fairly narrow, being 0.46 eV and 0.51 eV, respectively, for $CaMnGe_2O_6$ and $SrMnGe_2O_6$, which are

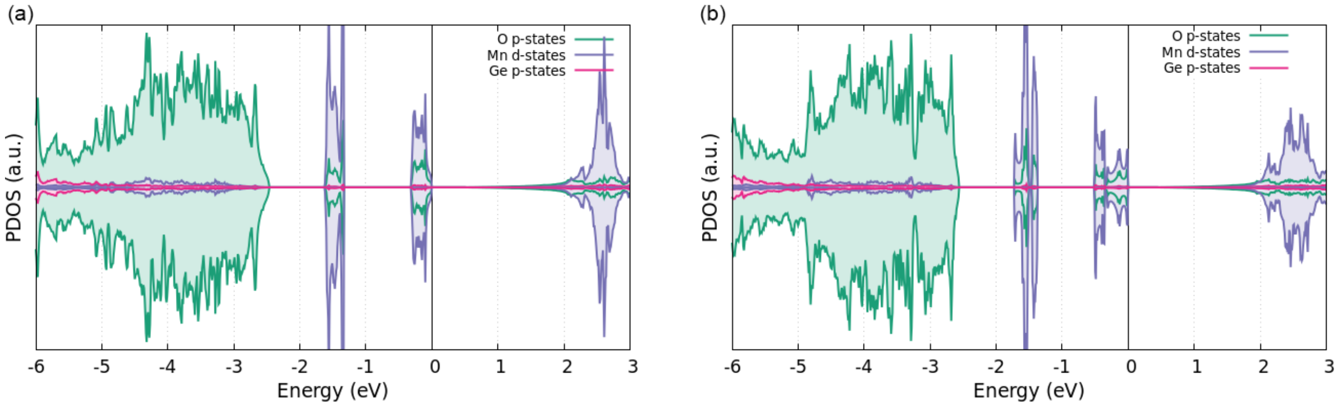

FIG. 2. Projected density of states for (a) $CaMnGe_2O_6$ and (b) $SrMnGe_2O_6$, computed with the PBE approximation. The Fermi level is set to zero and corresponds to the VBM.

narrower than what have been reported for similar Si-based compounds [7,45].

Since the band gap widths of these systems are likely underestimated in the absence of the Hubbard-U correction, we have also considered the PDOS by including the $U = 4$ eV correction on the Mn-3d states. These are shown in Fig. 3 along with the respective electronic band structures in a path along the high-symmetry points and directions of the BZ depicted in Fig. 4, generated with the SeeK-path tool [46,47] When including the U parameter and comparing to the PDOS results without this correction, differences are mainly evidenced at the VBM region, where the Mn-3d derived two narrow sets of bands observed in Fig. 2, now overlap and form one narrow set of bands for $CaMnGe_2O_6$ [Fig. 3(a)]. As for the $SrMnGe_2O_6$ system, the narrow bands are now energetically very close, almost forming one narrow band [Fig. 3(b)]. Moreover, these narrow bands are now dominated by a stronger hybridization between Mn-3d and O-p states. Since the inclusion of the U parameter localizes and positions the unoccupied narrow Mn-3d states higher in energy (between 5.0 and 5.5 eV), the bands around the CBM show slightly increased p hybridized states of O and Ge than when U correction is not considered.

The PBE + U theoretical band gaps are wider when compared to the previous case, with 1.82 and 1.70 eV for the $CaMnGe_2O_6$ and $SrMnGe_2O_6$ compounds, respectively, as can be observed in Table II. Despite this, the gap widths are still below the range of other similar Si-based clinopyroxenes [7,45]. We must stress that subtleties persist with respect to the analysis of the VBM, since the valence bands are quite flat, and thus the electronic bands along the different high-symmetry segments/points are energetically very close. Comparing to the band gaps reported in the theoretical works through GGA + U by Fakhera *et al.* [14] and Akter *et al.* [13], they both report a different nature for the band gaps, with both finding their respective studied systems as half-metallic and with significantly different widths for the band gaps (Akter *et al.* reported a 3.05 eV half-metallic gap for $CaMnGe_2O_6$, while Fakhera *et al.* reported a direct half-metallic gap for $SrMnGe_2O_6$), whereas we found the systems to be insulating. This is likely a result of their choice to perform the calculations with an FM configuration for the systems, whereas the systems are known experimentally to have an AFM ground state, moreover, the AFM configuration is also found to be more stable in the context of DFT calculations. This conclusion is further supported by the work reported by Temnikov *et al.* [12], who performed DFT simulations on the $CaMnGe_2O_6$ system considering an AFM alignment and, as with the present work, reported an insulating character for the system with a bandgap of ∼2 eV, similar to that obtained here.

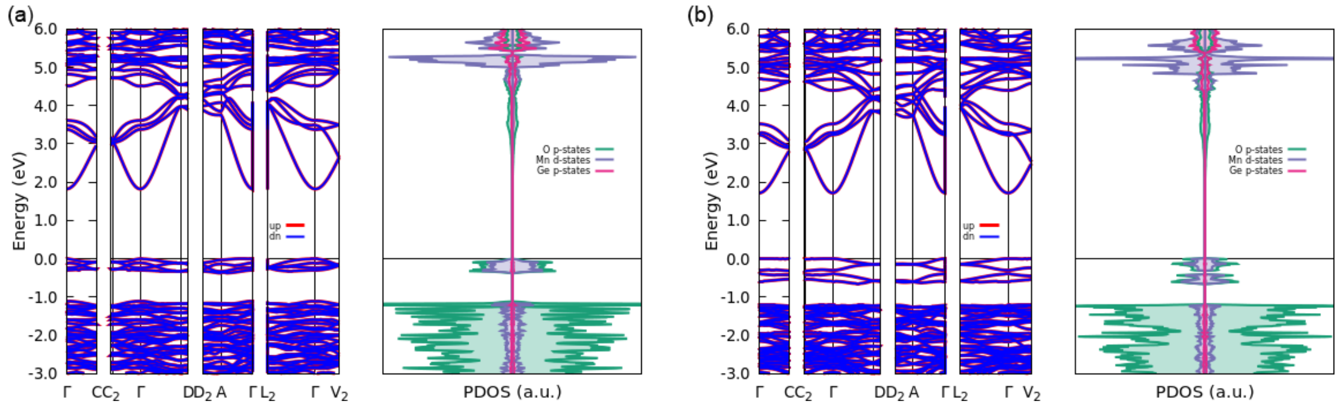

FIG. 3. (a) $CaMnGe_2O_6$ and (b) $SrMnGe_2O_6$ band structures in the high-symmetry directions of the BZ (left) and projected density of states (right), computed with PBE + U and antiferromagnetic ordering. The Fermi level is set to zero and matches the VBM.

TABLE II. Theoretical electronic indirect band gaps (E_g) and charge carriers effective masses m_e^* and m_h^* (in units of the electron mass $m_0 = 9.11 \times 10^{-31}$ kg) for the pristine and Cd-doped systems obtained with PBE + U. Values shown in shaded cells are those obtained with the HSE06 hybrid exchange-correlation functional. Experimental optical direct (dir.) and indirect (ind.) band gaps are also shown.

System	Theor. E_g (eV)	Expt. ind. E_g (eV)	Expt. dir. E_g (eV)	m_e^* (m_0)	m_h^* (m_0)
$SrMnGe_2O_6$	1.70	3.39(1)	3.66(2)	1.023	9.380 ($\Gamma \rightarrow D$)
	2.91				
$Sr_{0.875}Cd_{0.125}MnGe_2O_6$	1.55	3.28(6)	3.54(2)	1.028	58.223 ($\overline{C_2\Gamma} \rightarrow C_2$)
$Sr_{0.75}Cd_{0.25}MnGe_2O_6$	1.49	3.10(5)	3.33(2)	1.106	58.287 ($\overline{C_2\Gamma} \rightarrow C_2$)
	2.60				
$SrMn_{0.875}Cd_{0.125}Ge_2O_6$	1.56	3.33(2)	3.54(2)	1.057	40.062 ($\overline{C_2\Gamma} \rightarrow C_2$)
$SrMn_{0.75}Cd_{0.25}Ge_2O_6$	1.50	3.18(3)	3.59(3)	1.068	46.882 ($V_2 \rightarrow \Gamma$)
	2.66				
$CaMnGe_2O_6$	1.82	3.44(1)	3.78(2)	1.028	26.125 ($\overline{A\Gamma} \rightarrow A$)
	2.94				
$Ca_{0.875}Cd_{0.125}MnGe_2O_6$	1.59	3.30(1)	3.37(2)	1.028	67.562 ($\overline{A\Gamma} \rightarrow A$)
$Ca_{0.75}Cd_{0.25}MnGe_2O_6$	1.42	3.26(1)	3.48(1)	0.996	27.875 ($\overline{A\Gamma} \rightarrow A$)
	2.60				45.259 ($\overline{A\Gamma} \rightarrow \Gamma$)
$CaMn_{0.875}Cd_{0.125}Ge_2O_6$	1.58	3.26(1)	3.37(1)	1.033	18.704 ($\overline{A\Gamma} \rightarrow A$)
					68.128 ($\overline{A\Gamma} \rightarrow \Gamma$)
$CaMn_{0.75}Cd_{0.25}Ge_2O_6$	1.61	3.16(4)	3.49(3)	1.05	118.325 ($V_2 \rightarrow \Gamma$)
	2.77				

From experimental in-house diffuse reflectance measurements, we have obtained the optical indirect energy band gap widths of 3.43 and 3.38 eV for $CaMnGe_2O_6$ and $SrMnGe_2O_6$, respectively. Therefore, we have also computed the band-gap widths by employing the hybrid HSE06 approach for the exchange-correlation potential. These values are 2.94 and 2.91 eV, for $CaMnGe_2O_6$ and $SrMnGe_2O_6$, respectively, in much better agreement with experimental data (Table II).

From Fig. 3, one can observe that the VBM is much flatter than the CBM, which shows narrow parabolas around the zone center, indicating that the holes effective mass, m_h^*, is much larger than the electrons effective mass, m_e^*. Such an observation is an indication of a higher mobility of the electrons comparatively to the holes of the systems. Since the charge carrier effective mass is an essential parameter for the performance of photoelectric and photocatalytic activities [48], and also for semiconductor radiation detectors [49], we have considered further analyzing respective properties (Table II). Therefore, and to quantify the effective masses of holes and electrons, we employ the well-known definition of the effective mass as

$$m^* = \frac{\hbar^2}{\frac{\partial^2 E}{\partial k^2}}, \tag{5}$$

with the second derivative of the electronic dispersion relation being obtained from a quadratic fit around the energy range where the band edges are located.

In the case of $CaMnGe_2O_6$, we obtain a m_e^*, around the Γ point, very close to that of the free electrons, with $m_e^* = 1.028 m_0$ (where m_0 is the free electron mass of 9.11×10^{-31} kg). While for the hole carriers, and as expected by considering the flatness shape of the VBM, the mass of holes proved to be substantially larger (in absolute terms) with $m_h^* = 26.125 m_0$, calculated along the $\overline{A\Gamma} \rightarrow A$ high-symmetry segment (Table II).

The simulation of the (Ca, Sr)$MnGe_2O_6$ supercells containing Cd substitution at either Ca/Sr or Mn sites demonstrated that they are stable. The electronic band structures and the PDOS spectra were obtained for all doped systems and are displayed in Figs. 23–25 in Appendix C. The band gap transitions are summarized in Table II, where it can be observed that the doped structures show narrower indirect band gaps than the respective pristine compounds.

Regarding the $CaMnGe_2O_6$ supercells containing Cd substitution at the Ca site, we found that the electrons effective masses only yielded mild variation when compared to the pristine system. For the electrons, the m_e^* values showed very little to no increase, being $m_e^* = 0.996 m_0$ and $m_e^* = 1.028 m_0$, for the $Ca_{0.75}Cd_{0.25}MnGe_2O_6$ and $Ca_{0.875}Cd_{0.125}MnGe_2O_6$ systems, respectively. In the case of the holes, we observe that for the $Ca_{0.75}Cd_{0.25}MnGe_2O_6$ cell, and by comparing to the pristine system, m_h^* slightly increases along the $\overline{A\Gamma} \rightarrow \Gamma$ with $m_h^* = 45.259 m_0$, although showing similar values along $\overline{A\Gamma} \rightarrow A$ with $m_h^* = 27.875 m_0$.

Regarding the pristine $SrMnGe_2O_6$ structure, we found a similar value for the electron effective mass with $m_e^* = 1.023 m_0$. However, a significantly more parabolic dispersion relation at the VBM when compared to $CaMnGe_2O_6$, leading to a hole effective mass of $m_h^* = 9.380 m_0$, when considering the $\Gamma \rightarrow D$ segment. We must, however, state that since the valence band dispersion is quite asymmetric, the interpolation with a quadratic function did not yield a very accurate fit to the dispersion relation; therefore, the value of m_h^* should be understood more as an order of magnitude rather than a quantitative value.

It is observed, once again, that with the Cd substitution, there is only a mild variation of m_e^*, leading

TABLE III. Experimental (gray shaded cells) and theoretical EFG parameters for $SrMnGe_2O_6$ and $CaMnGe_2O_6$ related compounds. For the Cd compounds, theoretical values are at the Cd site.

System	$\lvert V_{zz}\rvert$ (V/Å^2)	η
EFG^{SMGO_1} (13 K)	120(1)	0.28(1)
EFG^{SMGO_2} (13 K)	20(1)	0.81(6)
$SrMnGe_2O_6$ Sr-site	64	0.54
$Sr_{0.875}Cd_{0.125}MnGe_2O_6$	108	0.14
$Sr_{0.75}Cd_{0.25}MnGe_2O_6$	103	0.14
$SrMnGe_2O_6$ Mn-site	14	0.32
$SrMn_{0.875}Cd_{0.125}Ge_2O_6$	21	0.74
$SrMn_{0.75}Cd_{0.25}Ge_2O_6$	22	0.67
EFG^{CMGO_1} (11 K)	130(1)	0.15(1)
EFG^{CMGO_2} (351 K)	10(2)	
$CaMnGe_2O_6$ Ca-site	34	0.52
$Ca_{0.875}Cd_{0.125}MnGe_2O_6$	109	0.01
$Ca_{075}Cd_{0.25}MnGe_2O_6$	108	0.02
$CaMnGe_2O_6$ Mn-site	8	0.49
$CaMn_{0.825}Cd_{0.125}Ge_2O_6$	12	0.21
$CaMn_{0.75}Cd_{0.25}Ge_2O_6$	12	0.31

to a slightly increased value of $m_e^* = 1.028m_0$ for $Sr_{0.875}Cd_{0.125}MnGe_2O_6$, and a more pronounced increase for the $Sr_{0.75}Cd_{0.25}MnGe_2O_6$ compound with $m_e^* = 1.106m_0$. As for the $SrMn_{0.75}Cd_{0.25}Ge_2O_6$ and $SrMn_{0.875}Cd_{0.125}Ge_2O_6$ systems, a slight increase of the effective masses is observed to $m_e^* = 1.068m_0$ and $m_e^* = 1.057m_0$, respectively. With respect to the m_h^*, we again note that due to the flat shape of the bands, a parabolic interpolation does not provide a dependable quantitative value, so we can only state with confidence that this value should remain of the same order as that of the pristine $SrMnGe_2O_6$ compound.

Concluding this analysis, we must state that such observed differences of the masses between the charge carriers is quite interesting because of the increased possibility to enhance the separation of the electron–hole pairs, and even of evidencing large electron and hole drift lengths [49], thus affecting the optoelectronic properties of the studied clinopyroxenes [50].

The DFT EFG calculations at all crystallographic positions were performed for the pristine $AMnGe_2O_6$ systems and for the supercells with Cd substitution, either at the A site or Mn site. These results, together with the ones obtained experimentally, are summarized in Table III and discussed in the next section. A more comprehensive list of computed values can be found in Appendix D, Table XIV. There, the EFG at each A, Mn, and Ge atomic position is presented for the pristine compounds alongside with the result for the Cd-doped systems.

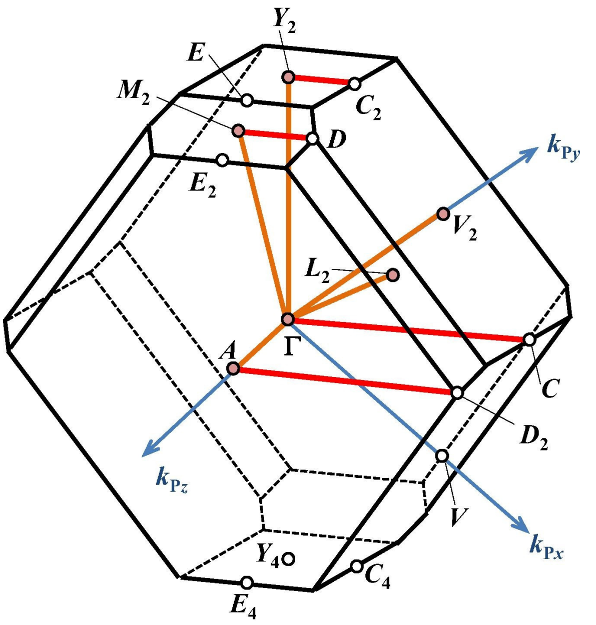

FIG. 4. Base-centered monoclinic lattice first Brillouin zone and respective high-symmetry points and directions. Adapted from Ref. [46].

B. Time-differential perturbed angular correlation

The EFG characterization, after ^{111m}Cd implantation, was performed in a wide range of temperatures for both $(Sr/Ca)MnGe_2O_6$ systems. To assess the consistency of the structural features before and after implantation, the pre- and postimplantation x-ray diffractograms are shown in Appendix D, Figs. 13 and 14. This study aimed to determine the location of implanted Cd in the $(Sr/Ca)MnGe_2O_6$ structure and to accurately describe the temperature dependence of the EFG in pristine samples. TDPAC measurements on the $SrMnGe_2O_6$ (SMGO) system were conducted at selected temperatures ranging from 13 to 902 K. Figure 5 shows a few representative experimental $\gamma - \gamma$ $R(t)$ functions obtained for the $SrMnGe_2O_6$ compound along with their corresponding Fourier transforms. Several models were tested to numerically obtain the best fit to the experimental $R(t)$ spectra before arriving at the presented model, wherein two distinct fractions (two distinct local environments) are evident across the whole temperature range, indicating the probes interacted with two distinct EFG distributions, henceforth referred to as EFG^{SMGO_1} and EFG^{SMGO_2}, and represented by the green and blue lines in Fig. 5, respectively.

The temperature behavior of the experimental $R(t)$ fit parameters of SMGO is displayed in Fig. 6. One can observe, in Fig. 6(a), green circles, that the V_{zz} value for the EFG^{SMGO_1} fraction has a noticeable increase at low temperatures, with increasing temperature, reaching a maximum; whereupon it starts to decrease. On the other hand, the axial asymmetry $\eta(1)$ parameter increases as the temperature increases, as displayed in Fig. 6(b) by the green circles. The aforementioned behavior of the V_{zz} is typically caused by a contribution from low-frequency phonon modes that leads to a linear decrease at high temperatures; as observed, though, the effects of the lattice volume expansion with temperature and structural relaxation around the probe also contribute to this behavior [51–53]. Regarding the axial asymmetry parameter $\eta(1)$ at the EFG^{SMGO_1} site, it displays an intermediate asymmetry, which increases as temperature raises.

For the EFG^{SMGO_2} fraction, depicted by the blue triagles in Fig. 6(a), the V_{zz} shows an atypical behavior of increasing as temperature also increases, though such behavior has nevertheless been reported in other compounds. Specifically, analogous behavior was experimentally observed

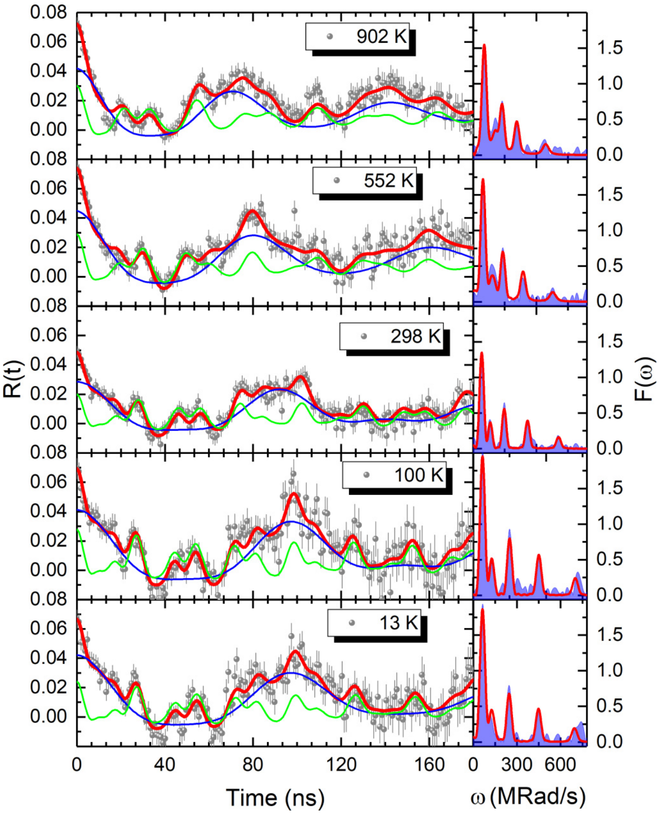

FIG. 5. Representative $R(t)$ spectra of $SrMnGe_2O_6$ and corresponding fits (left), as well as Fourier transforms (right). Green and blue lines represent two distinct EFG distributions, referred to in the text as EFG^{SMGO_1} and EFG^{SMGO_2}, respectively.

in the $A2_1am$ phase of $Ca_3Mn_2O_7$ for which DFT simulations indicated that such behavior is actually due to structural effects that prevail over the phonon contributions [54]. The asymmetry parameter $\eta(2)$ for the EFG^{SMGO_2} fraction, as displayed in Fig. 6(b) by the blue triangles, on the other hand, remains approximately constant, up to 474 K, whereupon an anomalous increase occurs. It is unclear if such behavior could be related to structural phenomena, as there are no measurements reported for temperatures above 350 K. Finally, it is worth noting that the probes distribution between both fraction remained fairly constant across the whole temperature range. This strongly suggests that Cd occupies two distinct lattice sites within the crystal and that both the crystallographic structure and Cd positions remain stable up to the highest measured temperature (900 K).

With respect to the $CaMnGe_2O_6$ (CMGO) system, the TDPAC measurements were likewise performed at selected temperatures, in the 11–898 K range. Representative fits to the experimental $R(t)$ perturbation functions for CMGO are presented in Fig. 7, along with the corresponding Fourier transforms. Similar to how the data from the previous compound was treated, several models were also tested to numerically obtain the best fit to the experimental $R(t)$ spectra. Distinctly from $SrMnGe_2O_6$, wherein two noticeable fractions are present across the whole temperature range, for the $CaMnGe_2O_6$ compound there is only one fraction present from low temperatures, up to 351 K, hereby referred to as EFG^{CMGO_1} and represented by the green lines in Fig. 7. It can be noticed in this figure that a second fraction, labeled EFG^{CMGO_2}, appears for temperatures above 351 K, represented by the blue lines. However, it is likely that this second fraction is likewise present at lower temperatures, but owing to the very small observable frequency associated with it, which is not well defined in the time window available in the TDPAC experiments, it is not possible to fit this fraction at lower temperatures. Even at high temperatures the EFG^{CMGO_2} fitting parameters nonetheless have an associated high uncertainty.

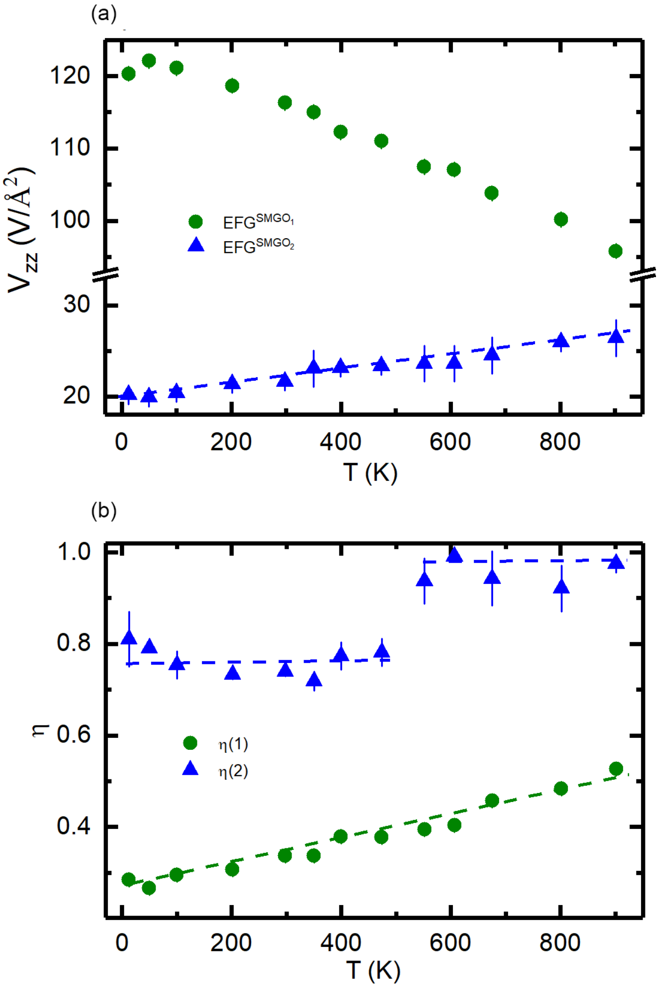

FIG. 6. Measured EFG parameters at the Cd probe in $SrMnGe_2O_6$: (a) V_{zz} and (b) η. The green circles correspond to the EFG^{SMGO_1} fraction and the blue triangles to the EFG^{SMGO_2}. The dashed lines are merely a guide to the eyes.

The temperature behavior of the fit parameters relative to the $CaMnGe_2O_6$ system are shown in Fig. 8. One can observe, in Fig. 8(a), green circles, that the EFG^{CMGO_1} distribution has a V_{zz} value of similar magnitude to EFG^{SMGO_1} [Fig. 6(a)], with an analogous decrease as temperature raises.

Also $\eta(1)$, displayed in Fig. 8(b), green circles, similarly increases with increasing temperature, when compared to SMGO $\eta(1)$ variation [Fig. 6(b)]. Similarly to what was observed for $SrMnGe_2O_6$, we note that the magnetic hyperfine interactions were not apparent in the fits to the experimental $R(t)$ functions.

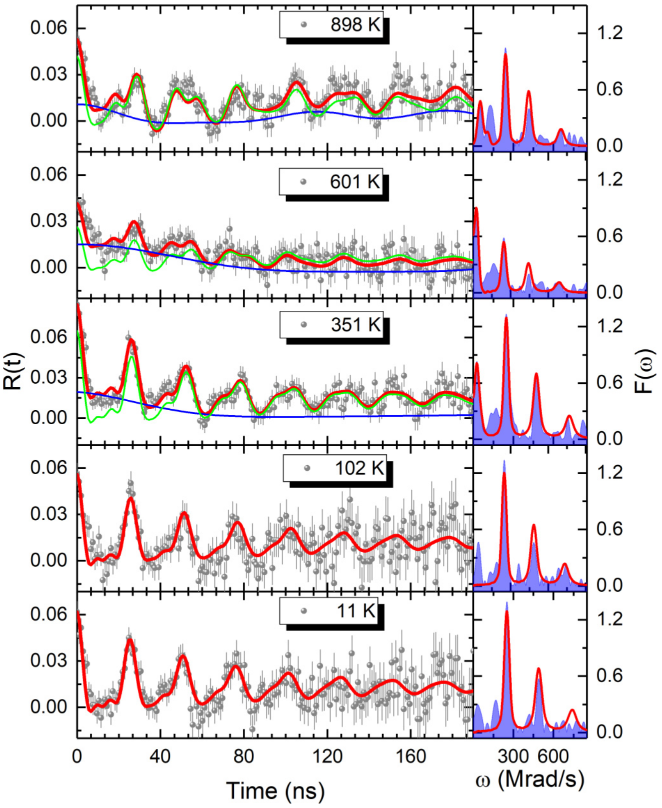

FIG. 7. Representative $R(t)$ spectra of $CaMnGe_2O_6$ and corresponding fits (left) as well as Fourier transforms (right). Green and blue lines represent two distinct EFG distributions, referred in the text as EFG^{CMGO_1} and EFG^{CMGO_2}, respectively.

To aid in the interpretation of these results, experimental data needs to be analyzed in comparison with the EFGs from DFT calculations. These EFGs are summarized in Table III. Comparing the EFG parameters for the experimental EFG^{SMGO_1} fraction of $SrMnGe_2O_6$ with those computed for the supercells with Cd substitution at the Sr site, where the 25% and 12.5% Cd dilutions were considered (unit cell and $1 \times 1 \times 2$ supercell, respectively), we may observe a very good agreement between V_{zz} and η. From the TDPAC measurements, we obtain for EFG^{SMGO_1} the values of $V_{zz} = 120$ V/Å^2 and $\eta = 0.28$; for the Cd probe nucleus for $Sr_{0.75}Cd_{0.25}MnGe_2O_6$ they are $V_{zz} = 103$ V/Å^2 and $\eta = 0.14$ and for $Sr_{0.875}Cd_{0.125}MnGe_2O_6$ these result as $V_{zz} = 108$ V/Å^2 and $\eta = 0.14$. Likewise, good agreement is also observed for the EFG^{SMGO_2} fraction of $SrMnGe_2O_6$ for the case of the Cd substitution at the Mn site. We obtain for the EFG^{SMGO_2} fraction the values of $V_{zz} = 20$ V/Å^2 and $\eta = 0.81$. From the DFT results, we get $V_{zz} = 22$ V/Å^2 and $\eta = 0.67$, and $V_{zz} = 21$ V/Å^2 and $\eta = 0.72$ for the $SrMn_{0.75}Cd_{0.25}Ge_2O_6$ and $SrMn_{0.875}Cd_{0.125}Ge_2O_6$ cells, respectively. Based on the obtained theoretical results, we may conclude that the supercells simulate quite well the experimental data when the Cd probe is considered, with the EFGs being in good agreement to the EFG^{SMGO_1} and EFG^{SMGO_2} experimental fractions, which correspond to the Cd probe replacing the Sr sites and the Mn sites, respectively, in the crystalline structure.

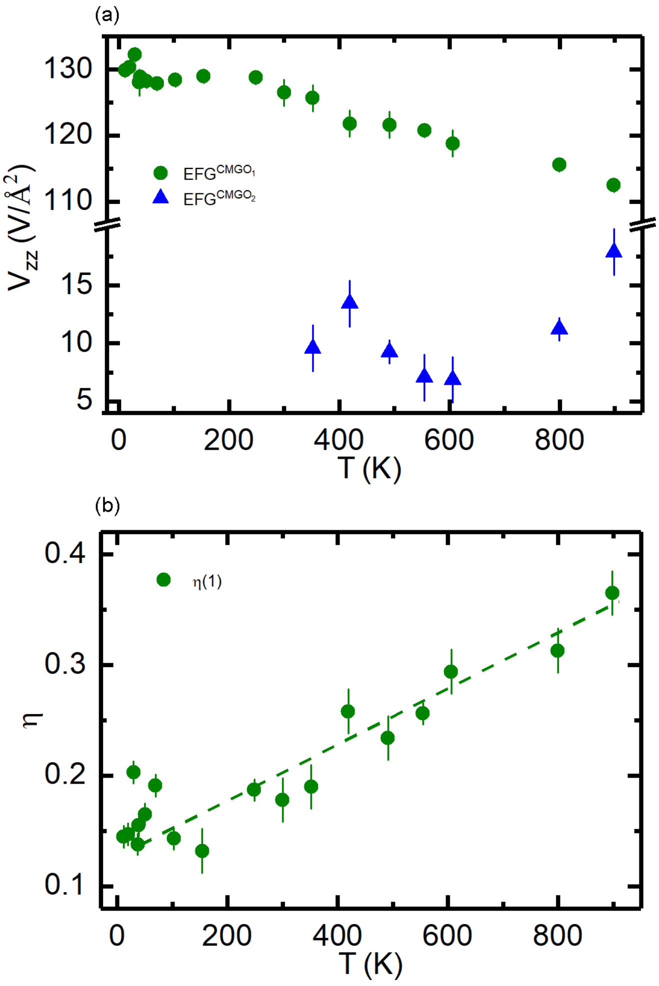

FIG. 8. Measured EFG parameters at the Cd probe in $CaMnGe_2O_6$: (a) V_{zz} and (b) η. The green circles correspond to the EFG^{CMGO_1} fraction and the blue triangles to the EFG^{CMGO_2}. The dashed lines are merely a guide to the eyes.

Similarly, this same correspondence seems to hold true for the $CaMnGe_2O_6$ compound. For the EFG^{CMGO_1} experimental fraction, we observe the values of $V_{zz} = 130$ V/Å^2 and $\eta = 0.15$, and for the DFT data we obtain values of $V_{zz} = 108$ (109) V/Å^2 and $\eta = 0.01$ (0.02) for Cd concentration of 1/4 (1/8) in the Ca atom position. The obtained theoretical EFGs are slightly lower than those of the experimental fraction; such is mostly evident for the asymmetry parameter, η. As for the EFG^{CMGO_2} fraction from the TDPAC experiments, the EFG result in $V_{zz} = 10$ V/Å^2 and an indeterminate η, whereas for the DFT diluted supercell of $CaMn_{0.825}Cd_{0.125}Ge_2O_6$ we have $V_{zz} = 12$ V/Å^2 and $\eta = 0.21$, similar to those obtained for $CaMn_{0.75}Cd_{0.25}Ge_2O_6$. It should be noted that in the cases where Cd was placed at a Mn site, the systems were treated as ferromagnetic, for the sake of computational simplicity. An antiferromagnetic calculation for the $CaMn_{0.875}Cd_{0.125}Ge_2O_6$ system was nevertheless performed to check how much of an effect the magnetic ordering might have on the computed EFG. Very similar results were obtained in both the ferromagnetic and antiferromagnetic calculations, with $V_{zz} = 12$ V/Å^2 and $\eta = 0.21$ in the former case and $V_{zz} = 13$ V/Å^2 and

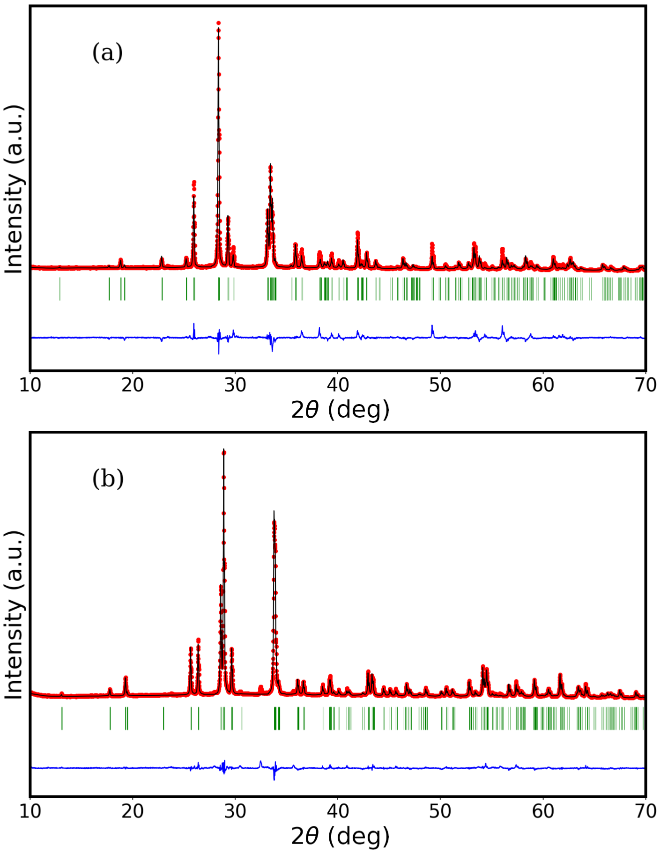

FIG. 9. Experimental XRD pattern (red dots), calculated XRD pattern based on the structure obtained from Rietveld refinement (black line), and difference between the two curves (blue line) of the (a) $Sr_{0.875}Cd_{0.125}MnGe_2O_6$ and (b) $Ca_{0.875}Cd_{0.125}MnGe_2O_6$. Green tick marks indicate the position of the Bragg reflections for the $C2/c$ space group.

$\eta = 0.37$ in the latter, thus showing that this approximation is reliable.

These results indicate that first-principles calculations combined with TDPAC spectroscopy provide a valuable tool to explain the observed two distinct local environments, indicating that Cd probes can in fact be distributed between the Sr or Ca sites and the Mn sites in the $SrMnGe_2O_6$ and $CaMnGe_2O_6$ basic compounds, respectively.

C. X-ray diffraction

Based on the comparison of TDPAC measurements with DFT calculations, which indicated that Cd probes occupy either the *A* or the Mn cation sites in pristine systems, and considering that *ab initio* calculations suggested Cd doping may impact the band gaps of these systems, we attempted to synthesize doped samples of $CaMnGe_2O_6$ and $SrMnGe_2O_6$ at the same concentrations as considered for the DFT calculations.

To gauge the phase purity of the samples, XRD measurements were performed, along with a Reitveld refinement that was done to obtain the lattice parameters and atomic positions of these compounds. The structural refinement was conducted using the room temperature XRD data, with the previously reported models for the parent compounds [2,6]. The x-ray data for $Sr_{0.875}Cd_{0.125}MnGe_2O_6$ and $Ca_{0.875}Cd_{0.125}MnGe_2O_6$ and their respective Rietveld refinements are shown in Fig. 9 while those for the remainder of the systems are in Appendix B.

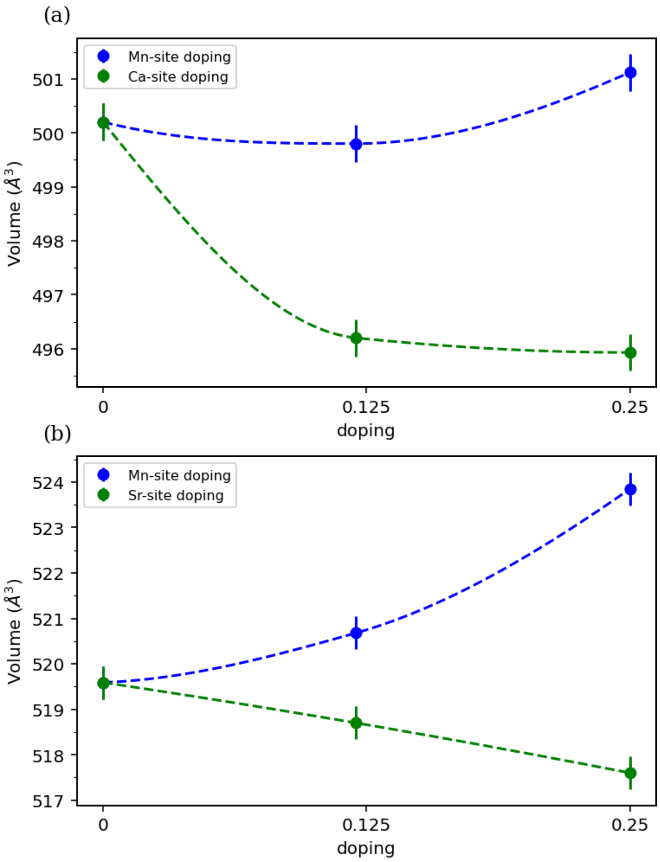

FIG. 10. Volume as a function of doping for (a) $CaMnGe_2O_6$, (b) $SrMnGe_2O_6$.

The x-ray measurements show all doped samples crystallized in the $C2/c$ space group, the same as the parent compounds, along with some minor impurity phases (the remaining experimental XRD patterns are shown in Appendix B). The lattice parameters and atomic positions are given in Tables V–XIII. The volume dependence on doping for the systems is represented in Fig. 10. A slight decrease in cell volume ($<0.9\%$) is observed by doping the Ca/Sr site, while a small increase (0.85%) is noticed when alloying at the manganese site. These trends align with expectations based on the atomic radii of the dopant elements.

It can be observed that the doping at the *A* site led to a much more significant reduction in cell volume in the $CaMnGe_2O_6$ system, relative to $SrMnGe_2O_6$. In contrast, doping at the Mn site had a more pronounced effect in increasing the volume of $SrMnGe_2O_6$ as compared to $CaMnGe_2O_6$. These observations may point toward the Cd dopants preferring the Ca over the Mn site in $CaMnGe_2O_6$, whereas in $SrMnG_2O_6$ the Sr site is more favorable for doping. Although according to structural data from Refs. [3,6] the MnO_6 octahedra in these systems have similar volumes, the octahedra are observed to be more distorted in $CaMnGe_2O_6$ than in $SrMnGe_2O_6$, and

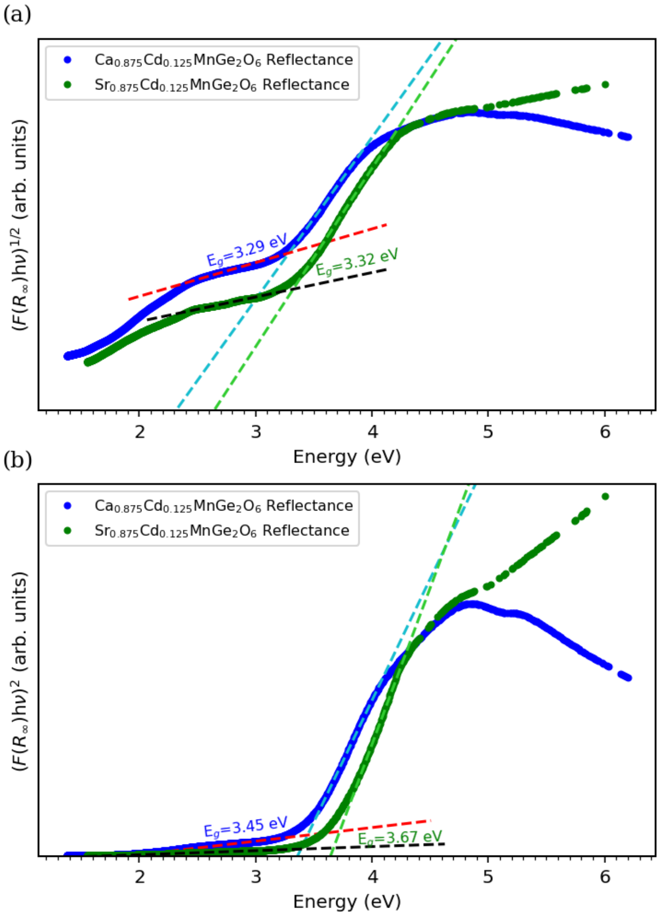

FIG. 11. Tauc's plot of (a) indirect and (b) direct band gap E_g for the $Ca_{0.875}Cd_{0.125}MnGe_2O_6$ and $Sr_{0.875}Cd_{0.125}MnGe_2O_6$ compounds. Dashed lines represent linear fits.

may therefore be less favorable of an environment for Cd. This is in agreement with the results from the TDPAC measurements, where the fraction identified as occupying the Ca site is well-defined and present across the whole temperature range, whereas the fraction that was identified as occupying the Mn site is only found at higher temperatures and is overall less clearly defined than the first one, likewise suggesting that the Ca site is less favorable for occupation by Cd atoms than the Mn site.

D. Reflectometry

To investigate the optical properties of synthesized compounds, we recorded the diffuse reflectance spectra in the UV-visible region 200–900 nm at room temperature.

Figure 11 illustrates representative Tauc plots of the Kubelka–Munk function for direct and indirect allowed transitions obtained from the diffuse reflectance spectra. The experimental data shows that the samples start to absorb for λ < 420 nm (> 2.7 eV), usually corresponding to the threshold of indirect optical band gap, leading to prompt e-/h+ recombination or only reaching the conduction band by adding extra energy from the crystalline (thermal) phonons. The absorption reaches maximum at λ ∼ 340 nm (∼ 3.6 eV), corresponding to the effective band gap or the edge of direct optical band gap. This photon energy can directly drive the photoexcited electrons to the conduction band (minimizing recombination) until filling the limited density of states available. Higher energy conduction bands (with limited DOS) are available between 4 and 5 eV. Above 5 eV, further transport mechanisms can be activated.After determining the intersection in energy of the linear fit to the fundamental absorption edge with the base line defined by a linear fit to the weak slope below the fundamental absorption, one obtains the values of the energy gap transition. The experimental change in the band gap width upon alloying with Cd at Ca/Sr or Mn sites, along with those

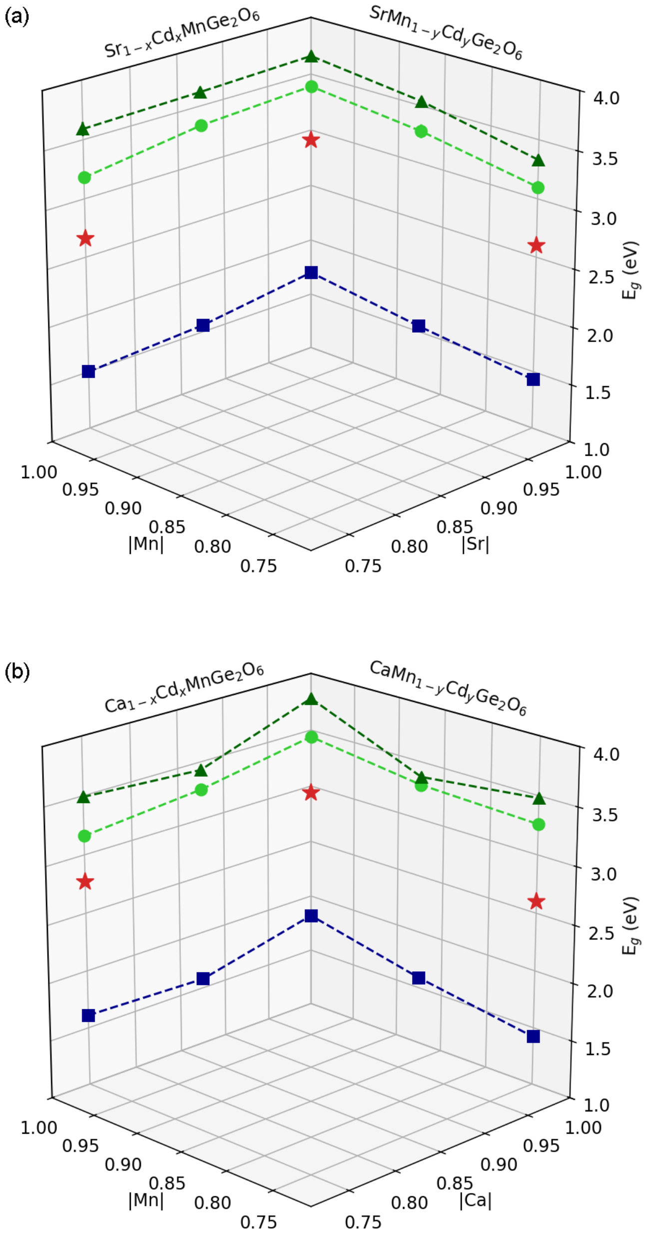

FIG. 12. Experimental direct (dark green triangles) and indirect (green circles) band gaps, along with the values obtained with DFT + U approach (blue squares) and HSE06 hybrid functional (red stars) as a function of Cd concentration x for (a) $SrMnGe_2O_6$ doped with Cd at the Sr and Mn sites (b) $CaMnGe_2O_6$ doped with Cd at the Ca and Mn sites.

obtained from PBE + U calculations, as well as calculations utilizing the HSE06 hybrid functional, are presented in Table II and shown in Fig. 12. The results showed that alloying with Cd in these systems lead to a reduction in band gap width, as predicted by the DFT calculations. Moreover, with the exception of doping at the Ca^{2+} site in $CaMnGe_2O_6$ where the band gap remained close to constant with increased Cd content, a further reduction was observed when increasing the Cd amount from 12.5% to 25%. Whereas the parent systems have band gaps that lie beyond the upper limit of the visible light spectrum, alloying with Cd at an amount of 25%, the band gap is lowered in value to lie within the spectrum of visible light.

IV. CONCLUSIONS

We have undertaken DFT calculations to obtain the structural and electronic properties of the AMnGe$_2$O$_6$ clinopyroxene systems, with A = Be, Mg, Ca, Sr. We found, through enthalpy of formation calculations, that Be- and Mg-based systems are not thermodynamically stable against dissociation into the stable constituent oxides $BeGeO_3$ or $MgGeO_3$ and $MnGeO_3$. On the other hand, Ca- and Sr-based systems are thermodynamically stable against dissociation and, accordingly, have been realized experimentally. From the PDOS, we found that the strongly correlated Mn 3d states form the narrow band close to the VBM together with the O p states. The CBM is composed mainly of low density hybridized p states of O and Ge and, for higher energies, the density of states significantly increases, forming a narrow resonant band that is mainly composed of the antibound unnocupied Mn 3d states. The theoretical electronic band gaps of $CaMnGe_2O_6$ and $SrMnGe_2O_6$ compounds, computed using the PBE + U approximation, were found to be significantly underestimated by comparison to the experimental optical gaps obtained through reflectometry, whereas calculations using the HSE06 hybrid functional were able to closely replicate the experimental results. The calculated effective masses of the charge carriers of the two studied pristine compounds show considerable differences, which implies that the separation of the electron–hole pairs can be enhanced, thus improving the photoelectric efficiency. By considering the Cd dopants, we do not observe much variation on the value of the charge carrier masses, whereas a decrease of the band-gap widths is observed.

Through the combination of theoretical *ab initio* calculations and TDPAC results, we could infer that the Cd probe in the AMnGe$_2$O$_6$ clinopyroxene compounds, with A = Ca, Sr, can replace the ion located at the A site as well as the Mn ion. Subsequently, the germanate clinopyroxene Cd alloys were successfully synthesized and experimentally characterized. The diffuse reflectance measurements show the possibility of tuning the band gap through Cd doping and the absorption for UV photons, with the possibility of tuning the absorption toward the upper limits of the visible spectrum through Cd doping, highlighting its potential applications in various fields.

ACKNOWLEDGMENTS

The authors acknowledge the support of the technical teams at ISOLDE for their exceptional work in delivering high-quality beams for the presented TDPAC measurements. The authors also acknowledge project NECL under NORTE-01-0145-FEDER-022096 and FCT Projects No. UIDP/04968/2020 [55], No. UIDB/04968/2020 [56], LaP-MET No. LA/P/0095/2020, No. POCI-01-0145-FEDER-029454, No. POCI-01-0145-FEDER-032527, No. CERN/FIS-TEC/0003/2021 [57] and No. 2024.00223.CERN [58]. Also, BMBF through Grants No. 05K16PGA and No. 05K22PGA, EU Horizon Europe Framework research and innovation program under Grant Agreement No. 101057511 (EURO-LABS) for supporting the IS679 ISOLDE-CERN experiment, and PRACE project with Reference No. 2021240118, with access to the Irene Skylake computer. R.P.M. acknowledges support from the Project HPC-EUROPA3 (INFRAIA-2016-1-730897), with the support of the EC Research Innovation Action under the H2020 Programme, with Reference No. HPC171030W and from FCT through the Ph.D. studentship with Reference No. 2020.08546.BD; in particular, the support of Doctor A. Stroppa and the hospitality provided by CNR-SPIN at the Department of Physical and Chemical Science of the University of L'Aquila (Italy) as well as computer resources and technical support provided by CINECA. R.P.M. also acknowledges computer resources and technical support from Minho Advanced Computing Center through Project No. CPCA/A1/460622/2021, financed by FCT. LVCA (Project No. 314884/2021-1) and HMP (Project No. 308438/2022-1) acknowledge funding from CNPq and support from FAPESP (Project No. 2022/10095-8). A.M.L.L. acknowledges the FCT 2021.04084.CEECIND [59] and E.L.d.S. the 2022.00082.CEECIND grants [60]. E.L.d.S. further acknowledges the High Performance Computing Chair—a R&D infrastructure (based at the University of Évora; PI: M. Avillez), endorsed by Hewlett Packard Enterprise, and involving a consortium of higher education institutions, research centers, enterprises, and public/private organizations.

APPENDIX A: FORMATION ENERGIES

The formation energies for the studied oxides of the AMnGe$_2$O$_6$ (A = Be, Mg, Ca, Sr) clinopyroxene series were calculated according to the following equation:

$$E_{\text{form}} = E_{A\text{MnGe}_2\text{O}_6} - E_{A\text{GeO}_3} - E_{\text{MnGeO}_3}, \tag{A1}$$

where $E_{A\text{MnGe}_2\text{O}_6}$, $E_{A\text{GeO}_3}$, and E_{MnGeO_3} are the total electronic energies obtained from DFT + U calculations, per formula unit (f.u.), which are summarized in Table IV.

TABLE IV. Electronic total energies of the $AMnGe_2O_6$ clinopyroxene compounds (A = Be, Mg, Ca, Sr) and of their respective constituent $AGeO_3$ and $MnGeO_3$ oxides.

System	Energy (eV/f.u.)
$SrMnGe_2O_6$	−19433.62
$CaMnGe_2O_6$	−17709.36
$MgMnGe_2O_6$	−17815.41
$BeMnGe_2O_6$	−15984.00
$SrGeO_3$	−9540.40
$CaGeO_3$	−7816.06
$MgGeO_3$	−7922.42
$BeGeO_3$	−6091.01
$MnGeO_3$	−9893.11

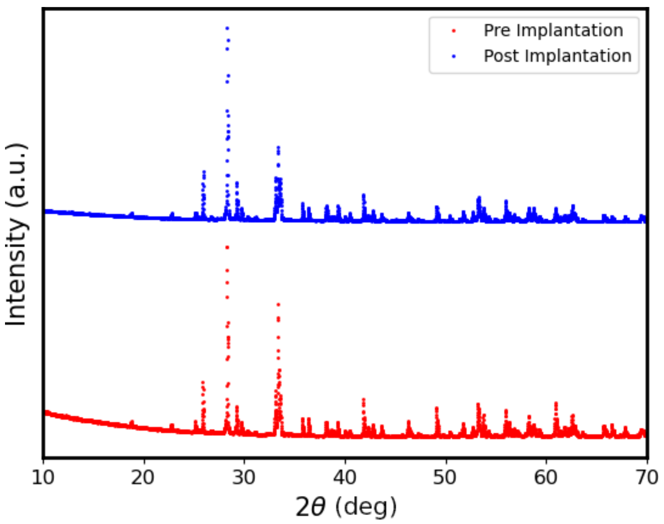

FIG. 14. Experimental XRD pattern for $SrMnGe_2O_6$, before (red dots) and after (blue dots) implantation with Cd.

APPENDIX B: X-RAY DIFFRACTION

The XRD measurements for the pristine $CaMnGe_2O_6$ and $SrMnGe_2O_6$ systems, before and after implantation with ^{111m}Cd probes, are presented in Figs. 13 and 14. The x-ray data for $Ca_{1-x}Cd_xMnGe_2O_6$ and $CaCd_xMn_{1-x}Ge_2O_6$ ($x = 0.125, 0.25$) are presented, respectively, in Figs. 15–18 and for $Sr_{1-x}Cd_xMnGe_2O_6$ and $SrCd_xMn_{1-x}Ge_2O_6$ ($x = 0.125, 0.25$) the x-ray data are shown in Figs. 19–22, along with their respective Rietveld refinements. All refined structural parameters are shown in Tables V to XII. Table XIII displays the refined lattice parameters for all Cd-related compounds.

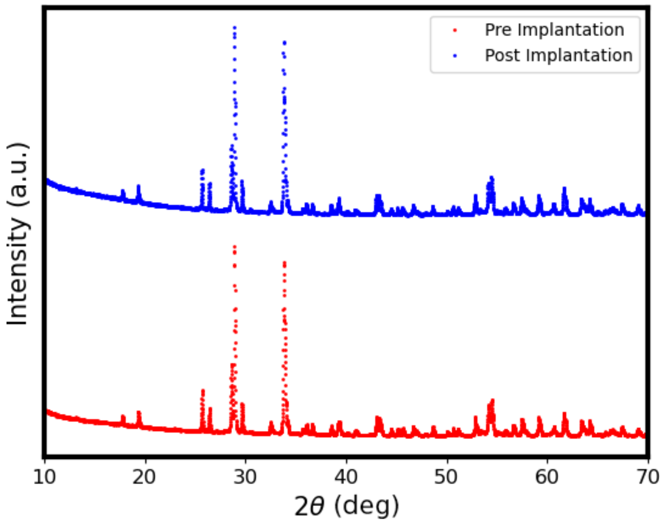

FIG. 13. Experimental XRD pattern for $CaMnGe_2O_6$, before (red dots) and after (blue dots) implantation with Cd.

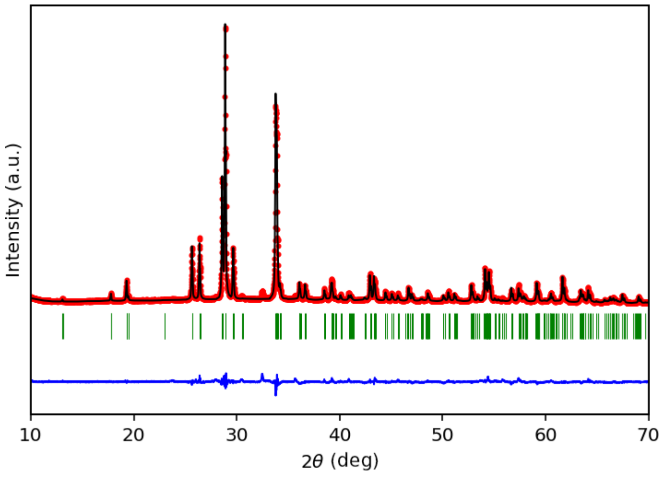

FIG. 15. Experimental XRD pattern (red dots), calculated XRD pattern based on the structure obtained from Rietveld refinement (black line), and the two curve difference (blue line) of the $Ca_{0.875}Cd_{0.125}MnGe_2O_6$ compound. Green tick marks indicate the position of the Bragg reflections for the $C2/c$ space group.

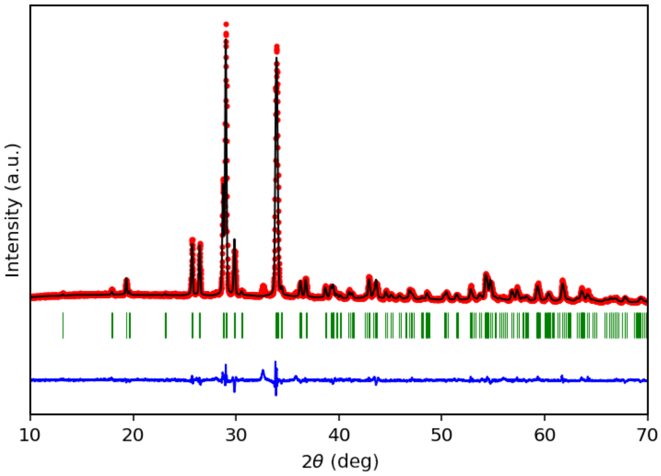

FIG. 16. Experimental XRD pattern (red dots), calculated XRD pattern based on the structure obtained from Rietveld refinement (black line), and the two curve difference (blue line) of the $Ca_{0.75}Cd_{0.25}MnGe_2O_6$ compound. Green tick marks indicate the position of the Bragg reflections for the $C2/c$ space group.

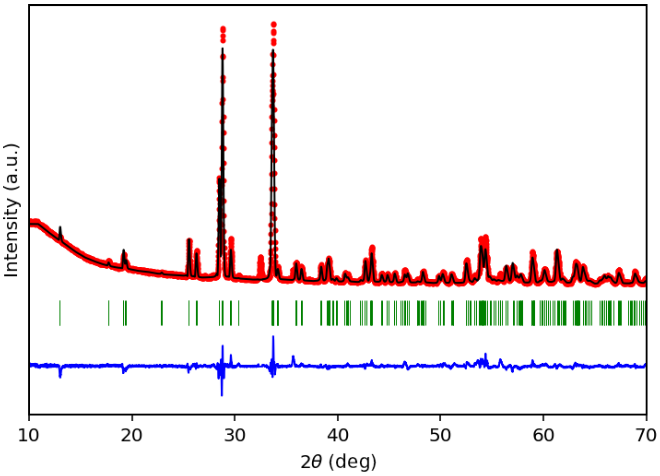

FIG. 18. Experimental XRD pattern (red dots), calculated XRD pattern based on the structure obtained from Rietveld refinement (black line), and difference between the two curves (blue line) of the $CaMn_{0.75}Cd_{0.25}Ge_2O_6$ compound. Green tick marks indicate the position of the Bragg reflections for the $C2/c$ space group.

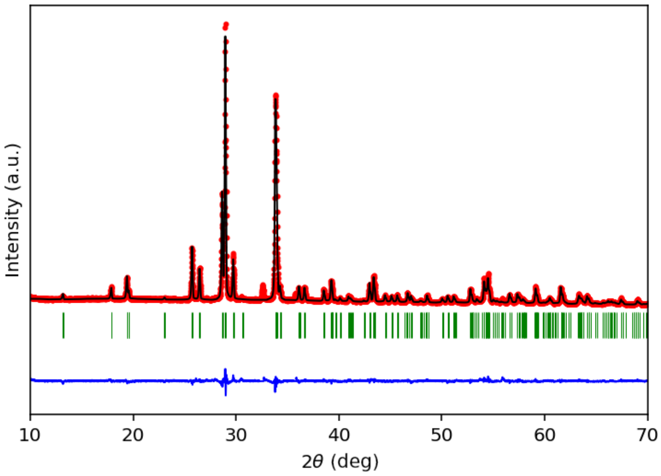

FIG. 17. Experimental XRD pattern (red dots), calculated XRD pattern based on the structure obtained from Rietveld refinement (black line), and the two curve difference (blue line) of the $CaMn_{0.875}Cd_{0.125}Ge_2O_6$ compound. Green tick marks indicate the position of the Bragg reflections for the $C2/c$ space group.

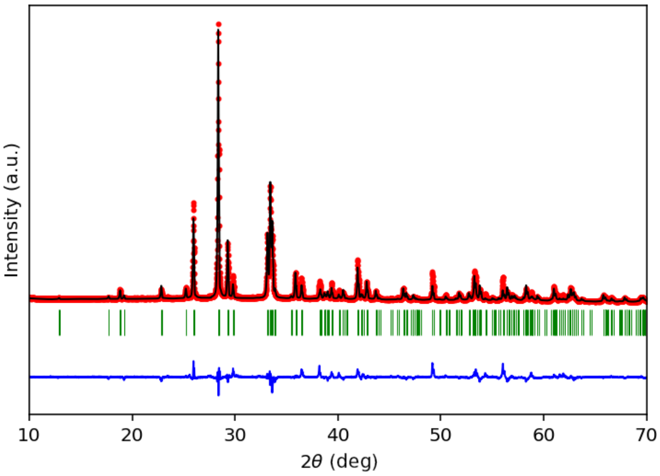

FIG. 19. Experimental XRD pattern (red dots), calculated XRD pattern based on the structure obtained from Rietveld refinement (black line), and difference between the two curves (blue line) of the $Sr_{0.875}Cd_{0.125}MnGe_2O_6$ compound. Green tick marks indicate the position of the Bragg reflections for the $C2/c$ space group.

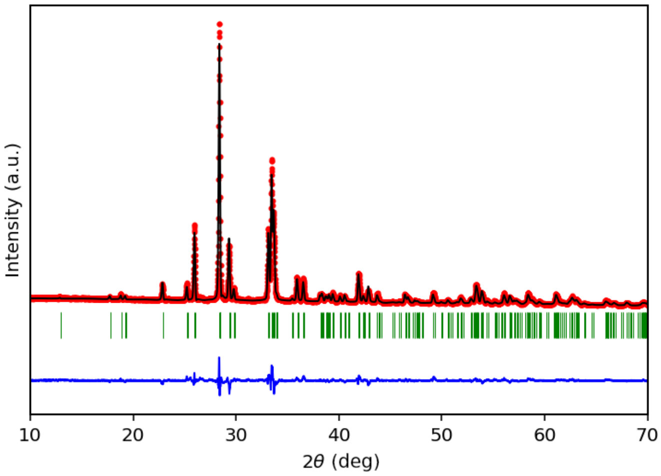

FIG. 20. Experimental XRD pattern (red dots), calculated XRD pattern based on the structure obtained from Rietveld refinement (black line), and difference between the two curves (blue line) of the $Sr_{0.75}Cd_{0.25}MnGe_2O_6$ compound. Green tick marks indicate the position of the Bragg reflections for the $C2/c$ space group.

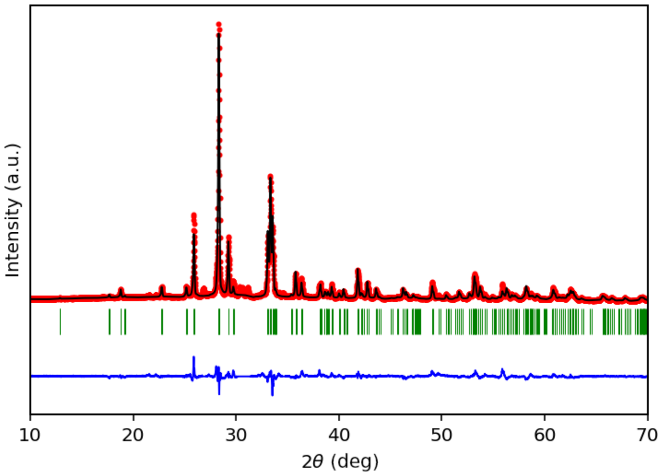

FIG. 21. Experimental XRD pattern (red dots), calculated XRD pattern based on the structure obtained from Rietveld refinement (black line), and difference between the two curves (blue line) of the $SrMn_{0.875}Cd_{0.125}Ge_2O_6$ compound. Green tick marks indicate the position of the Bragg reflections for the $C2/c$ space group.

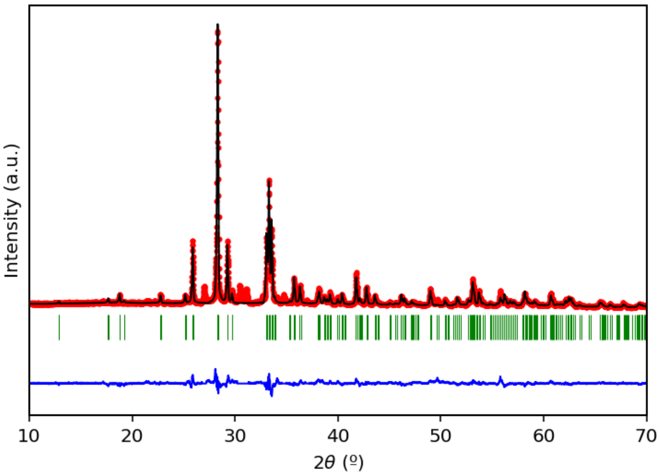

FIG. 22. Experimental XRD pattern (red dots), calculated XRD pattern based on the structure obtained from Rietveld refinement (black line), and difference between the two curves (blue line) of the $SrMn_{0.75}Cd_{0.25}Ge_2O_6$ compound. Green tick marks indicate the position of the Bragg reflections for the $C2/c$ space group.

TABLE V. Refined structural parameters for $Ca_{0.875}Cd_{0.125}MnGe_2O_6$ compound. Space group $C2/c$ (No. 15); $\chi^2 = 4.42$; $R_{wp} = 5.51$; $R_{\mathrm{Bragg}} = 7.21$.

	x/a	y/b	z/c	U_{iso}(Å^2)
Ca/Cd	0.0	0.302(1)	0.25	0.050(1)
Mn	0.0	0.906(1)	0.25	0.032(1)
Ge	0.288(1)	0.095(1)	0.233(1)	0.038(1)
O(1)	0.108(1)	0.103(1)	0.138(1)	0.035(1)
O(2)	0.379(1)	0.256(1)	0.363(1)	0.028(1)
O(3)	0.350(1)	0.025(1)	0.977(1)	0.029(1)

TABLE VI. Refined structural parameters for $Ca_{0.75}Cd_{0.25}MnGe_2O_6$. Space group $C2/c$ (No. 15); $\chi^2 = 3.33$; $R_{wp} = 6.19$; $R_{\rm Bragg} = 6.97$.

	x/a	y/b	z/c	$U_{\rm iso}(\text{Å}^2)$
Ca/Cd	0.0	0.299(1)	0.25	0.073(1)
Mn	0.0	0.910(1)	0.25	0.033(1)
Ge	0.288(1)	0.096(1)	0.230(1)	0.051(1)
O(1)	0.111(1)	0.093(1)	0.141(1)	0.032(2)
O(2)	0.375(1)	0.252(1)	0.346(1)	0.058(3)
O(3)	0.358(1)	0.041(1)	0.974(1)	0.046(3)

TABLE VII. Refined structural parameters for $CaMn_{0.875}Cd_{0.125}Ge_2O_6$. Space group $C2/c$ (No. 15); $\chi^2 = 3.22$; $R_{wp} = 5.40$; $R_{\rm Bragg} = 6.73$.

	x/a	y/b	z/c	$U_{\rm iso}(\text{Å}^2)$
Ca	0.0	0.304(1)	0.25	0.036(1)
Mn/Cd	0.0	0.907(1)	0.25	0.070(1)
Ge	0.287(1)	0.097(1)	0.233(1)	0.047(1)
O(1)	0.115(1)	0.104(1)	0.148(1)	0.053(2)
O(2)	0.368(1)	0.253(1)	0.358(1)	0.023(1)
O(3)	0.358(1)	0.023(1)	0.983(1)	0.049(2)

TABLE VIII. Refined structural parameters for $CaMn_{0.75}Cd_{0.25}Ge_2O_6$. Space group $C2/c$ (No. 15); $\chi^2 = 7.73$; $R_{wp} = 5.75$; $R_{\rm Bragg} = 12.3$.

	x/a	y/b	z/c	$U_{\rm iso}(\text{Å}^2)$
Ca	0.0	0.293(1)	0.25	0.0003(1)
Mn/Cd	0.0	0.902(1)	0.25	0.005(1)
Ge	0.288(1)	0.096(1)	0.234(1)	0.001(1)
O(1)	0.112(1)	0.097(1)	0.151(1)	0.009(2)
O(2)	0.367(1)	0.263(1)	0.372(1)	0.008(3)
O(3)	0.378(1)	0.034(1)	0.981(1)	0.08(2)

TABLE IX. Refined structural parameters for the $Sr_{0.875}Cd_{0.125}MnGe_2O_6$ compound. Space group $C2/c$ (No. 15); $\chi^2 = 7.21$; $R_{wp} = 9.67$; $R_{\rm Bragg} = 15.1$.

	x/a	y/b	z/c	$U_{\rm iso}(\text{Å}^2)$
Sr/Cd	0.0	0.306(1)	0.25	0.039(1)
Mn	0.0	0.907(1)	0.25	0.033(1)
Ge	0.284(1)	0.090(1)	0.217(1)	0.053(1)
O(1)	0.108(1)	0.079(1)	0.123(1)	0.030(4)
O(2)	0.391(1)	0.241(1)	0.367(2)	0.099(6)
O(3)	0.338(1)	0.013(1)	0.990(2)	0.036(5)

TABLE X. Refined structural parameters for the $Sr_{0.75}Cd_{0.25}MnGe_2O_6$ compound. Space group $C2/c$ (No. 15); $\chi^2 = 4.45$; $R_{wp} = 7.26$; $R_{\rm Bragg} = 10.7$.

	x/a	y/b	z/c	$U_{\rm iso}(\text{Å}^2)$
Sr/Cd	0.0	0.303(1)	0.25	0.081(1)
Mn	0.0	0.908(1)	0.25	0.052(1)
Ge	0.285(1)	0.093(1)	0.224(1)	0.067(1)
O(1)	0.105(1)	0.087(1)	0.135(1)	0.044(3)
O(2)	0.376(1)	0.258(1)	0.339(1)	0.103(4)
O(3)	0.347(1)	0.037(1)	0.995(1)	0.072(4)

TABLE XI. Refined structural parameters for $SrMn_{0.875}Cd_{0.125}Ge_2O_6$ compound. Space group $C2/c$ (No. 15); $\chi^2 = 6.46$; $R_{wp} = 8.46$; $R_{\rm Bragg} = 12.2$.

	x/a	y/b	z/c	$U_{\rm iso}(\text{Å}^2)$
Sr	0.0	0.3057(3)	0.25	0.0426(11)
Mn/Cd	0.0	0.9065(4)	0.25	0.0572(15)
Ge	0.2831(2)	0.092(1)	0.214(1)	0.054(1)
O(1)	0.101(1)	0.089(1)	0.132(1)	0.019(3)
O(2)	0.382(1)	0.248(1)	0.357(2)	0.087(5)
O(3)	0.343(1)	0.009(1)	0.987(1)	0.019(4)

TABLE XII. Refined structural parameters for $SrMn_{0.75}Cd_{0.25}Ge_2O_6$ compound. Space group $C2/c$ (No. 15); $\chi^2 = 5.87$; $R_{wp} = 9.43$; $R_{\rm Bragg} = 12.9$.

	x/a	y/b	z/c	$U_{\rm iso}(\text{Å}^2)$
Sr	0.0	0.307(1)	0.25	0.052(1)
Mn/Cd	0.0	0.906(1)	0.25	0.087(1)
Ge	0.284(1)	0.092(1)	0.214(1)	0.066(1)
O(1)	0.095(1)	0.090(1)	0.135(1)	0.029(3)
O(2)	0.369(1)	0.240(1)	0.360(1)	0.054(5)
O(3)	0.343(1)	0.009(1)	0.982(1)	0.029(4)

TABLE XIII. Refined lattice parameters for the $C2/c$ AMnGe$_2$O$_6$ (A = Ca, Sr) clinopyroxene compounds where Cd substitutes A or Mn ions.

Compound	a (Å)	b (Å)	c (Å)	β (deg)
$Ca_{0.875}Cd_{0.125}MnGe_2O_6$	10.247(1)	9.161(1)	5.454(1)	104.247(1)
$Ca_{0.75}Cd_{0.25}MnGe_2O_6$	10.222(1)	9.198(1)	5.439(1)	104.083(1)
$CaMn_{0.875}Cd_{0.125}Ge_2O_6$	10.272(1)	9.181(1)	5.466(1)	104.167(1)
$CaMn_{0.75}Cd_{0.25}Ge_2O_6$	10.265(1)	9.211(1)	5.458(1)	104.042(1)
$Sr_{0.875}Cd_{0.125}MnGe_2O_6$	10.344(1)	9.415(1)	5.507(1)	104.736(1)
$Sr_{0.75}Cd_{0.25}MnGe_2O_6$	10.329(1)	9.423(1)	5.500(1)	104.762(1)
$SrMn_{0.875}Cd_{0.125}Ge_2O_6$	10.356(1)	9.429(1)	5.511(1)	104.638(1)
$SrMn_{0.75}Cd_{0.25}Ge_2O_6$	10.378(1)	9.455(1)	5.516(1)	104.543(1)

APPENDIX C: ELECTRONIC BAND DISPERSION OF THE Cd DOPED SYSTEMS

Figures 23–25 present the band structures and the density of states for the *A*$MnGe_2O_6$ (A = Ca, Sr) clinopyroxene compounds where *A* or Mn atoms are substituted by Cd ions.

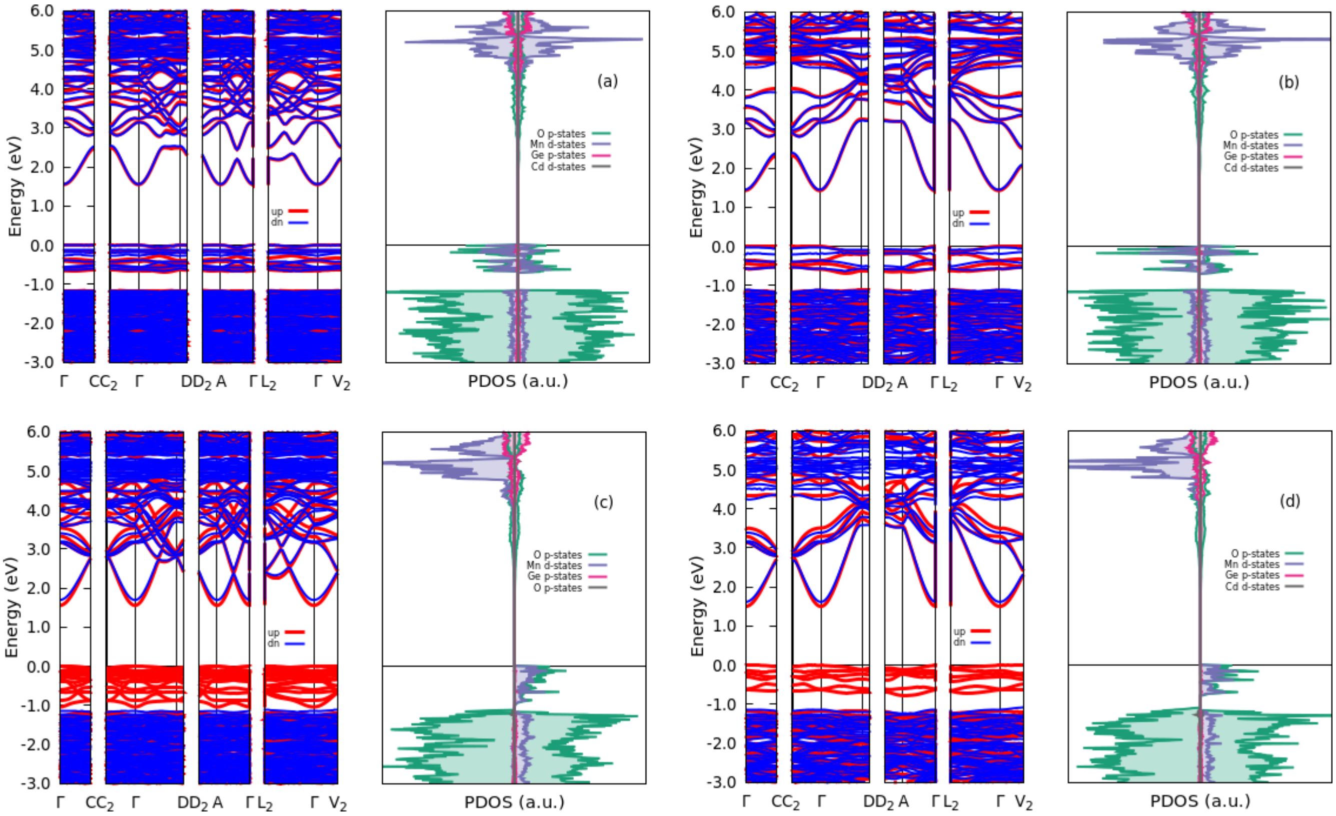

FIG. 23. Electronic band structure (left) and density of states (right) for (a) $Sr_{0.875}Cd_{0.125}MnGe_2O_6$ with antiferromagnetic ordering; (b) $Sr_{0.75}Cd_{0.25}MnGe_2O_6$ with antiferromagnetic ordering; (c) $SrMn_{0.875}Cd_{0.125}Ge_2O_6$ with ferromagnetic ordering; and (d) $SrMn_{0.75}Cd_{0.25}Ge_2O_6$ with ferromagnetic ordering.

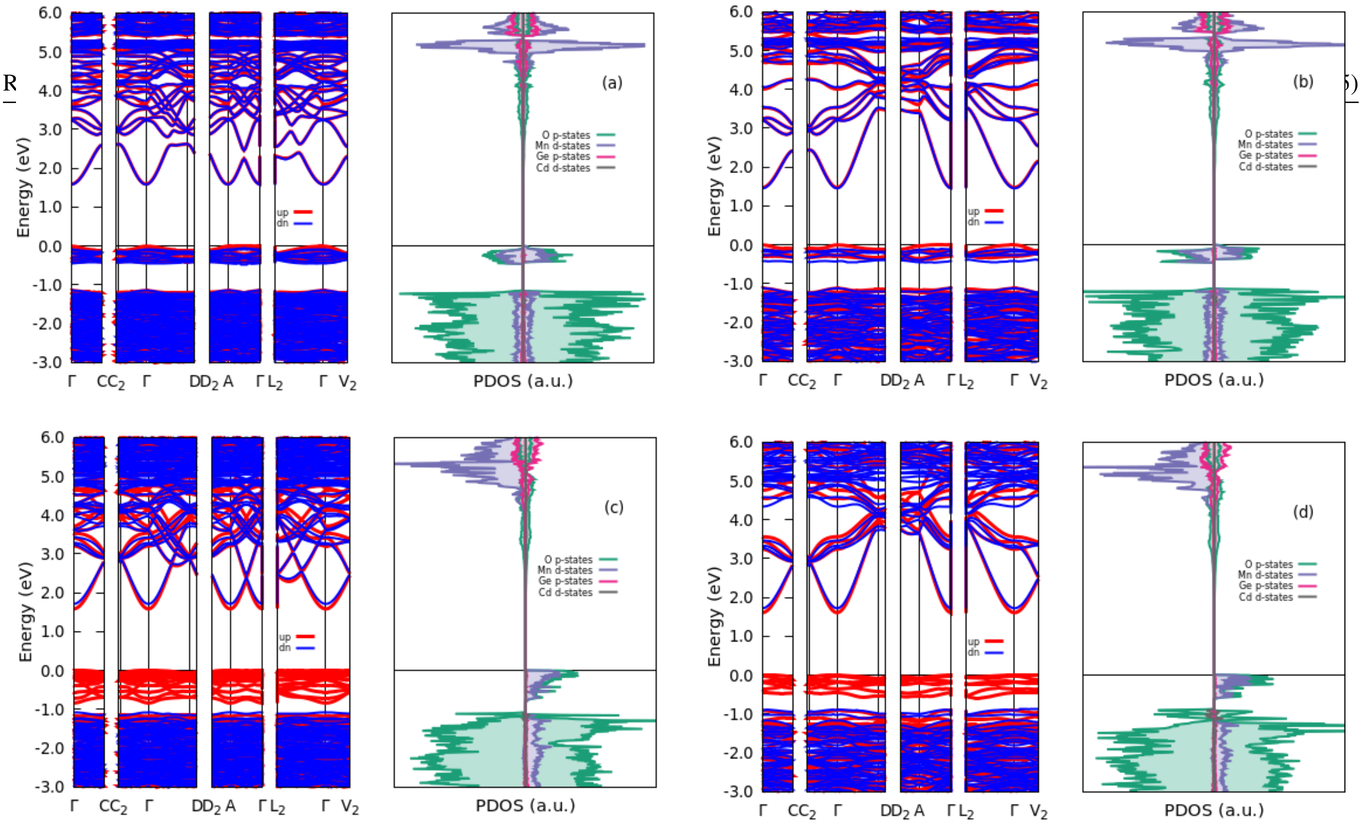

FIG. 24. Electronic band structure (left) and density of states (right) for: (a) $Ca_{0.875}Cd_{0.125}MnGe_2O_6$ with antiferromagnetic ordering; (b) $Ca_{0.75}Cd_{0.25}MnGe_2O_6$ with antiferromagnetic ordering; (c) $CaMn_{0.875}Cd_{0.125}Ge_2O_6$ with ferromagnetic ordering; (d) $CaMn_{0.75}Cd_{0.25}Ge_2O_6$ with ferromagnetic ordering.

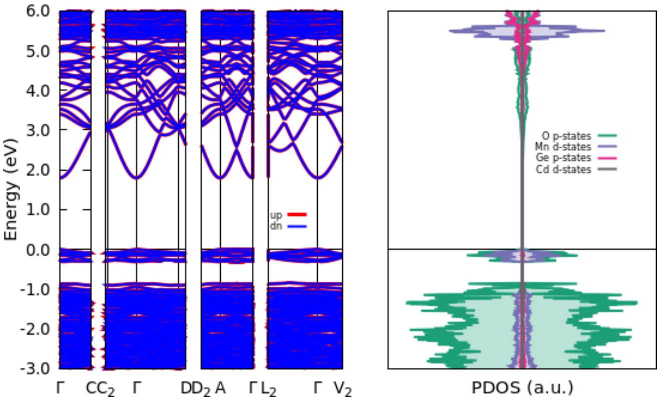

FIG. 25. Electronic band structure and density of states for $CaMn_{0.75}Cd_{0.25}Ge_2O_6$ with antiferromagnetic ordering.

APPENDIX D: ELECTRIC FIELD GRADIENT PARAMETERS

The calculated EFG parameters are presented in Table XIV. From these results, we can observe that the EFGs at the Ge nuclei were only slightly affected by the Cd substitution, as evidenced by the fact that the symmetry of the Ge sites remained quite similar to $SrMnGe_2O_6$ and $CaMnGe_2O_6$ basic compounds after Cd substitution. The same cannot be said for the Sr/Ca and Mn sites, which in many cases deviated substantially.

TABLE XIV. Computational EFG parameters at the Sr, Ca, Mn, Ge, and Cd nuclei for $SrMnGe_2O_6$, $SrMnGe_2O_6$:Cd_{Sr}, and $SrMnGe_2O_6$:Cd_{Mn}, $CaMnGe_2O_6$, $CaMnGe_2O_6$:Cd_{Ca}, and $SrMnGe_2O_6$:Cd_{Mn} compounds. $|V_{zz}|$ is given in V/Å^2 units.

System	EFG	Cd	Sr(1)	Sr(2)	Sr(3)	Sr(4)	Mn(1)	Mn(2)	Mn(3)	Mn(4)	Ge(1)	Ge(2)	Ge(3)	Ge(4)
$SrMnGe_2O_6$	$\|V_{zz}\|$		64				14				99			
	η		0.54				0.32				0.70			
$Sr_{0.875}Cd_{0.125}MnGe_2O_6$	$\|V_{zz}\|$	108	61	62	63	66	10	19	17	12	101	97	102	101
	η	0.14	0.46	0.71	0.53	0.83	0.64	0.98	0.44	0.84	0.60	0.64	0.64	0.69
$Sr_{0.75}Cd_{0.25}MnGe_2O_6$	$\|V_{zz}\|$	103	59	65	64		19	17	14	15	99	103	91	85
	η	0.14	0.88	0.82	0.66		0.42	0.75	0.60	0.16	0.55	0.64	0.55	0.67
$SrMn_{0.875}Cd_{0.125}Ge_2O_6$	$\|V_{zz}\|$	21	57	67	64	68	14	14	11	14	99	99	101	100
	η	0.74	0.47	0.63	0.57	0.59	0.28	0.46	0.63	0.35	0.71	0.69	0.69	0.69
$SrMn_{0.75}Cd_{0.25}Ge_2O_6$	$\|V_{zz}\|$	22	59	64	69	66	15	10	15		99	101	100	102
	η	0.67	0.56	0.59	0.63	0.64	0.58	0.61	0.23		0.71	0.67	0.73	0.69
System	EFG	Cd	Ca(1)	Ca(2)	Ca(3)	Ca(4)	Mn(1)	Mn(2)	Mn(3)	Mn(4)	Ge(1)	Ge(2)	Ge(3)	Ge(4)
$CaMnGe_2O_6$	$\|V_{zz}\|$		34				8				96			
	η		0.52				0.49				0.64			
$Ca_{0.875}Cd_{0.125}MnGe_2O_6$	$\|V_{zz}\|$	109	33	35	34	38	5	8	11	9	99	97	98	99
	η	0.01	0.45	0.34	0.45	0.33	0.43	0.30	0.69	0.93	0.52	0.60	0.60	0.60
$Ca_{0.75}Cd_{0.25}MnGe_2O_6$	$\|V_{zz}\|$	108	35	38	35		2	12	11	8	99	100	96	86
	η	0.02	0.13	0.27	0.29		0.09	0.11	0.15	0.95	0.50	0.58	0.44	0.67
$CaMn_{0.875}Cd_{0.125}Ge_2O_6$	$\|V_{zz}\|$	12	30	37	36	36	7	7	10	7	98	97	99	97
	η	0.21	0.42	0.41	0.38	0.39	0.76	0.92	0.34	0.82	0.63	0.61	0.60	0.66
$CaMn_{0.75}Cd_{0.25}Ge_2O_6$	$\|V_{zz}\|$	12	31	37	38	37	7	10	8		97	99	98	100
	η	0.31	0.42	0.39	0.40	0.39	0.37	0.38	0.96		0.63	0.58	0.64	0.59

---

[1] S. V. Streltsov and D. I. Khomskii, Electronic structure and magnetic properties of pyroxenes (Li, Na) TM (Si, Ge)$_2$O$_6$: Low-dimensional magnets with 90° bonds, Phys. Rev. B **77**, 064405 (2008).

[2] L. Ding, C. V. Colin, C. Darie, and P. Bordet, SrMGe$_2$O$_6$ (M = Mn, Co): A family of pyroxene compounds displaying multiferroicity, J. Mater. Chem. C **4**, 4236 (2016).

[3] C. V. Colin, L. Ding, E. Ressouche, J. Robert, N. Terada, F. Gay, P. Lejay, V. Simonet, C. Darie, P. Bordet, and S. Petit, Incommensurate spin ordering and excitations in multiferroic SrMnGe$_2$o$_6$, Phys. Rev. B **101**, 235109 (2020).

[4] S. Jodlauk, P. Becker, J. A. Mydosh, D. I. Khomskii, T. Lorenz, S. V. Streltsov, D. C. Hezel, and L. Bohatý, Pyroxenes: A new class of multiferroics, J. Phys.: Condens. Matter **19**, 432201 (2007).

[5] I. Kim, B.-G. Jeon, D. Patil, S. Patil, G. Nénert, and K. H. Kim, Observation of multiferroic properties in pyroxene NaFeGe$_2$O$_6$, J. Phys.: Condens. Matter **24**, 306001 (2012).

[6] L. Ding, C. V. Colin, C. Darie, J. Robert, F. Gay, and P. Bordet, One-dimensional short-range magnetic correlations in the magnetoelectric pyroxene CaMnGe$_2$O$_6$, Phys. Rev. B **93**, 064423 (2016).

[7] M. Legesse, H. Park, F. El Mellouhi, S. N. Rashkeev, S. Kais, and F. H. Alharbi, Improved photoactivity of pyroxene silicates by cation substitutions, ChemPhysChem **19**, 943 (2018).

[8] A. Torres, F. J. Luque, J. Tortajada, and M. E. Arroyo-de Dompablo, Analysis of minerals as electrode materials for Ca-based rechargeable batteries, Sci. Rep. **9**, 9644 (2019).

[9] S. Zhou, G. King, D. O. Scanlon, M. T. Sougrati, and B. C. Melot, Low temperature preparation and electrochemical properties of LiFeSi$_2$O$_6$, J. Electrochem. Soc. **161**, A1642 (2014).

[10] L. Jin, S. Peng, A. N. Rutherford, X. Xu, D. Ni, C. Yang, Y. J. Byeon, W. Xie, H. Zhou, X. Dai, and R. J. Cava, A pyroxene-based quantum magnet with multiple magnetization plateaus, Sci. Adv. **10**, eadp4685 (2024).

[11] P. A. Maksimov, A. V. Ushakov, A. F. Gubkin, G. J. Redhammer, S. M. Winter, A. I. Kolesnikov, A. M. dos Santos, Z. Gai, M. A. McGuire, A. Podlesnyak, and S. V. Streltsov, Cobalt-based pyroxenes: A new playground for Kitaev physics, Proc. Natl. Acad. Sci. USA **121**, e2409154121 (2024).

[12] F. V. Temnikov, E. V. Komleva, Z. V. Pchelkina, and S. V. Streltsov, Mechanism of ferromagnetic ordering of Mn chains in CaMnGe$_2$O$_6$ clinopyroxene, JETP Lett. **110**, 595 (2019).

[13] T. Akter, J. Islam, K. Hossain, and R. A. Rabu, First-principles investigation of half-metallic CaTGe$_2$O$_6$ (T = Mn, Fe, Co) clinopyroxenes: Potential for spintronics and optoelectronics applications, Heliyon **11**, e41315 (2025).

[14] F. Fakhera, K. Hossain, M. S. Khanom, M. K. Hossain, and F. Ahmed, Understanding the impact of Y^{2+} (Y = Mn, Fe, and Co) cations on physical properties of SrYGe$_2$O$_6$ clinopyroxene: A DFT insight, J. Phys. Chem. Solids **173**, 111112 (2023).

[15] P. Giannozzi, S. Baroni, N. Bonini, M. Calandra, R. Car, C. Cavazzoni, D. Ceresoli, G. L. Chiarotti, M. Cococcioni, I. Dabo, A. Dal Corso, S. de Gironcoli, S. Fabris, G. Fratesi, R. Gebauer, U. Gerstmann, C. Gougoussis, A. Kokalj, M. Lazzeri, L. Martin-Samos *et al.*, QUANTUM ESPRESSO: A modular and open-source software project for quantum simulations of materials, J. Phys.: Condens. Matter **21**, 395502 (2009).

[16] P. Giannozzi, O. Andreussi, T. Brumme, O. Bunau, M. B. Nardelli, M. Calandra, R. Car, C. Cavazzoni, D. Ceresoli, M. Cococcioni, N. Colonna, I. Carnimeo, A. D. Corso, S. de Gironcoli, P. Delugas, R. A. DiStasio, Jr., A. Ferretti, A. Floris, G. Fratesi, G. Fugallo *et al.*, Advanced capabilities for materials modeling with QUANTUM ESPRESSO, J. Phys.: Condens. Matter **29**, 465901 (2017).

[17] P. E. Blöchl, Projector augmented-wave method, Phys. Rev. B **50**, 17953 (1994).

[18] A. Dal Corso, Pseudopotentials periodic table: From H to Pu, Comput. Mater. Sci. **95**, 337 (2014).

[19] J. P. Perdew, K. Burke, and M. Ernzerhof, Generalized gradient approximation made simple, Phys. Rev. Lett. **77**, 3865 (1996).

[20] Data retrieved from the Materials Project for SrMn(GeO$_3$)$_2$ (mp-1208680) from database version v2022.10.28.

[21] A. Jain, S. P. Ong, G. Hautier, W. Chen, W. D. Richards, S. Dacek, S. Cholia, D. Gunter, D. Skinner, G. Ceder, and K. A. Persson, Commentary: The materials project: A materials genome approach to accelerating materials innovation, APL Mater. **1**, 011002 (2013).

[22] M. Cococcioni and S. de Gironcoli, Linear response approach to the calculation of the effective interaction parameters in the LDA + U method, Phys. Rev. B **71**, 035105 (2005).

[23] K. Hummer, J. Harl, and G. Kresse, Heyd-Scuseria-Ernzerhof hybrid functional for calculating the lattice dynamics of semiconductors, Phys. Rev. B **80**, 115205 (2009).

[24] R. M. Wentzcovitch, Invariant molecular-dynamics approach to structural phase transitions, Phys. Rev. B **44**, 2358 (1991).

[25] J. H. Kim, K. Levin, R. Wentzcovitch, and A. Auerbach, Electron-phonon interactions in the high-temperature superconductors, Phys. Rev. B **44**, 5148 (1991).

[26] R. M. Wentzcovitch, J. L. Martins, and G. D. Price, *Ab initio* Molecular dynamics with variable cell shape: Application to MgSiO$_3$, Phys. Rev. Lett. **70**, 3947 (1993).

[27] T. Charpentier, The PAW/GIPAW approach for computing NMR parameters: A new dimension added to NMR study of solids, Solid State Nucl. Magn. Reson. **40**, 1 (2011).

[28] P. Raghavan, Table of nuclear moments, At. Data Nucl. Data Tables **42**, 189 (1989).

[29] T. Butz, Analytic perturbation functions for static interactions in perturbed angular correlations of γ-rays, Hyperfine Interact. **52**, 189 (1989).

[30] G. Schatz and A. Weidinger, *Nuclear Condensed Matter Physics: Nuclear Methods and Applications* (John Wiley, Hoboken, New Jersey, 1996), p. 280.

[31] A. M. L. Lopes, J. P. Araújo, J. J. Ramasco, V. S. Amaral, R. Suryanarayanan, and J. G. Correia, Percolative transition on ferromagnetic insulator manganites: Uncorrelated to correlated polaron clusters, Phys. Rev. B **73**, 100408(R) (2006).

[32] N. P. Barradas, M. Rots, A. A. Melo, and J. C. Soares, Magnetic anisotropy and temperature dependence of the hyperfine fields of ^{111}Cd in single-crystalline cobalt, Phys. Rev. B **47**, 8763 (1993).

[33] J. G. Correia, NNFIT the pac manual (1992).

[34] J. G. Correia, NNFIT and FFT upgrades (2018).

[35] R. L. Rasera and G. L. Catchen, Perturbed angular correlation (PAC) spectroscopy as a tool for the study of ferroelectrics, Ferroelectrics **150**, 151 (1993).

[36] J. Rodríguez-Carvajal, Recent advances in magnetic structure determination by neutron powder diffraction, Phys. B: Condens. Matter **192**, 55 (1993).

[37] J. Rodriguez-Cavajal, Recent developments of the program FULLPROF (International Union of Crystallography Newsletter, 2001), Vol. 26.

[38] J. Rodriguez-Carvajal, FULLPROF: A program for rietveld refinement and pattern matching analysis, in *Satellite Meeting on Powder Diffraction of the XV congress of the IUCr* (Toulouse, France, 1990), Vol. 127.

[39] J. Tauc, R. Grigorovici, and A. Vancu, Optical properties and electronic structure of amorphous germanium, Physica Status Solidi (B) **15**, 627 (1966)

[40] E. A. Davis and N. F. Mott, Conduction in non-crystalline systems V. Conductivity, optical absorption and photoconductivity in amorphous semiconductors, The Philosophical Magazine: A Journal of Theoretical Experimental and Applied Physics **22**, 0903 (1970)

[41] N. F. Mott, E. A. Davis, and K. Weiser, Electronic processes in non-crystalline materials (1940), https://api.semanticscholar.org/CorpusID:136959916.

[42] P. Kubelka and F. Munk, Ein beitrag zur optik der farbanstriche, Z. Tech. Phys **12**, 593 (1931).

[43] P. Makuła, M. Pacia, and W. Macyk, How to correctly determine the band gap energy of modified semiconductor photocatalysts based on UV–vis spectra, J. Phys. Chem. Lett. **9**, 6814 (2018).

[44] P. Haas, F. Tran, and P. Blaha, Calculation of the lattice constant of solids with semilocal functionals, Phys. Rev. B **79**, 085104 (2009).

[45] S. V. Streltsov, J. McLeod, A. Moewes, G. J. Redhammer, and E. Z. Kurmaev, Electronic properties of pyroxenes NaCrSi$_2$O$_6$ and NaFeSi$_2$O$_6$, Phys. Rev. B **81**, 045118 (2010).

[46] Y. Hinuma, G. Pizzi, Y. Kumagai, F. Oba, and I. Tanaka, Band structure diagram paths based on crystallography, Comput. Mater. Sci. **128**, 140 (2017).

[47] A. Togo, K. Shinohara, and I. Tanaka, `Spglib`: A software library for crystal symmetry search, Sci. Technol. Adv. Mater.: Methods **4**, 2384822 (2024).

[48] X. Liu and K. Sohlberg, Role of effective carrier mass in the photocatalytic efficiency of La-doped NaTaO$_3$, Comput. Mater. Sci. **123**, 1 (2016).

[49] E. Y. Lee, R. B. James, R. Olsen, and H. Hermon, Compensation and trapping in CdZnTe radiation detectors studied by thermoelectric emission spectroscopy, thermally stimulated conductivity, and current-voltage measurements, J. Electron. Mater. **28**, 766 (1999).

[50] J.-R. Zhang, X.-Z. Deng, B. Gao, L. Chen, C.-T. Au, K. Li, S.-F. Yin, and M.-Q. Cai, Theoretical study on the intrinsic properties of In_2Se_3/MoS_2 as a photocatalyst driven by near-infrared, visible and ultraviolet light, Catal. Sci. Technol. **9**, 4659 (2019).

[51] H. Bayer, Zur theorie der spin-gitterrelaxation in molekülkristallen, Z. Phys. **130**, 227 (1951).

[52] T. Kushida, The influence of lattice vibration on the pure quadrupole line, J. Sci. Hiroshima Univ., Ser. A **19**, 327 (1955).

[53] T. Kushida, G. Benedek, and N. Bloembergen, Dependence of the pure quadrupole resonance frequency on pressure and temperature, Phys. Rev. **104**, 1364 (1956).

[54] P. Rocha-Rodrigues, S. S. M. Santos, I. P. Miranda, G. N. P. Oliveira, J. G. Correia, L. V. C. Assali, H. M. Petrilli, J. P. Araújo, and A. M. L. Lopes, $Ca_3Mn_2O_7$ structural path unraveled by atomic-scale properties: A combined experimental and *ab initio* study, Phys. Rev. B **101**, 064103 (2020).

[55] https://doi.org/10.54499/UIDP/04968/2020.

[56] https://doi.org/10.54499/UIDB/04968/2020.

[57] https://doi.org/10.54499/CERN/FIS-TEC/0003/2021.

[58] https://doi.org/10.54499/2024.00223.CERN.

[59] https://doi.org/10.54499/2021.04084.CEECIND/CP1655/CT0002.

[60] https://doi.org/10.54499/2022.00082.CEECIND/CP1719/CT0001.